



**HAL**  
open science

## Three-dimensional Lead Iodide Perovskitoid Hybrids with High X-ray Photoresponse

Xiaotong Li, Yihui He, Mikael Kepenekian, Peijun Guo, Weijun Ke, Jacky Even, Claudine Katan, Constantinos C Stoumpos, Richard Schaller, Mercouri G Kanatzidis

► **To cite this version:**

Xiaotong Li, Yihui He, Mikael Kepenekian, Peijun Guo, Weijun Ke, et al.. Three-dimensional Lead Iodide Perovskitoid Hybrids with High X-ray Photoresponse. *Journal of the American Chemical Society*, 2020, 142 (14), pp.6625-6637. 10.1021/jacs.0c00101 . hal-02509572

**HAL Id: hal-02509572**

**<https://hal.science/hal-02509572v1>**

Submitted on 14 May 2020

**HAL** is a multi-disciplinary open access archive for the deposit and dissemination of scientific research documents, whether they are published or not. The documents may come from teaching and research institutions in France or abroad, or from public or private research centers.

L'archive ouverte pluridisciplinaire **HAL**, est destinée au dépôt et à la diffusion de documents scientifiques de niveau recherche, publiés ou non, émanant des établissements d'enseignement et de recherche français ou étrangers, des laboratoires publics ou privés.

# Three-dimensional Lead Iodide Perovskitoid Hybrids with High X-ray Photoresponse

Xiaotong Li,<sup>†</sup> Yihui He,<sup>†</sup> Mikael Kepenekian,<sup>§</sup> Peijun Guo,<sup>‡</sup> Weijun Ke,<sup>†</sup> Jacky Even,<sup>||</sup> Claudine Katan,<sup>§</sup> Constantinos C. Stoumpos,<sup>∇</sup> Richard D. Schaller,<sup>†,‡</sup> and Mercouri G. Kanatzidis<sup>\*,†</sup>

<sup>†</sup>Department of Chemistry, Northwestern University, 2145 Sheridan Road, Evanston, Illinois 60208, United States

<sup>§</sup>Univ Rennes, ENSCR, INSA Rennes, CNRS, ISCR (Institut des Sciences Chimiques de Rennes), UMR 6226, Rennes F-35000, France

<sup>‡</sup>Center for Nanoscale Materials, Argonne National Laboratory, 9700 South Cass Avenue, Lemont, Illinois 60439, United States

<sup>||</sup>Univ Rennes, INSA Rennes, CNRS, Institut FOTON, UMR 6082, Rennes F-35000, France

<sup>∇</sup>Department of Materials Science and Technology, Voutes Campus, University of Crete, Heraklion GR-70013, Greece

## Abstract

Large organic A cations cannot stabilize the 3D perovskite  $AMX_3$  structure because they cannot be accommodated in the cubo-octahedral cage (do not follow the Goldschmidt tolerance factor rule), and they generally template low-dimensional structures. Here we report that the large di-cation aminomethylpyridinium (AMPY), can template novel 3D structures which resemble conventional perovskites. They have the formula  $(xAMPY)M_2I_6$  ( $x = 3$  or  $4$ ,  $M = Sn^{2+}$  or  $Pb^{2+}$ ) which is doubled the  $AMX_3$  formula. However, because of the steric requirement of the Goldschmidt tolerance factor rule, it is impossible for  $(xAMPY)M_2I_6$  to form proper perovskite structures. Instead, a combination of corner-sharing and edge-sharing connectivity is adopted in these compounds leading to the new 3D structures. DFT calculations reveal that the compounds are indirect-bandgap semiconductors with direct bandgaps presenting at slightly higher energies and dispersive electronic bands. The bandgaps of the Sn and Pb compounds are  $\sim 1.7$  eV and 2.0 eV, respectively, which is slightly higher than the corresponding  $AMI_3$  3D perovskites. The Raman spectra for the compounds are diffuse, with a broad rising central peak at very low frequencies around  $0\text{ cm}^{-1}$ , a feature that is characteristic of dynamical lattices, highly anharmonic, and dissipative vibrations very similar to the 3D  $AMX_3$  perovskites. Devices of  $(3AMPY)Pb_2I_6$  crystals exhibit clear photoresponse under ambient light without applied bias, reflecting a high carrier mobility ( $\mu$ ) and long carrier lifetime ( $\tau$ ). The devices also exhibit sizable X-ray generated photocurrent with a high  $\mu\tau$  product of  $\sim 1.2 \times 10^{-4}\text{ cm}^2/\text{V}$  and an X-ray sensitivity of  $207\ \mu\text{C}\cdot\text{Gy}^{-1}\cdot\text{cm}^{-2}$ .

1  
2  
3 **Keywords:** Metal halide hybrids, mixed cations, anomalous bandgap behavior, photoresponse, X-  
4 ray detector.  
5  
6  
7  
8  
9  
10  
11  
12  
13  
14  
15  
16  
17  
18  
19  
20  
21  
22  
23  
24  
25  
26  
27  
28  
29  
30  
31  
32  
33  
34  
35  
36  
37  
38  
39  
40  
41  
42  
43  
44  
45  
46  
47  
48  
49  
50  
51  
52  
53  
54  
55  
56  
57  
58  
59  
60

## Introduction

Three-dimensional (3D) hybrid halide perovskites have achieved tremendous success in photovoltaic devices<sup>1-3</sup> owing to their defect tolerance, long carrier lifetime and low trap density.<sup>4-6</sup> These properties also enable photodetector,<sup>7</sup> x-ray detection<sup>8</sup> and  $\gamma$ -ray detection applications<sup>9-11</sup>. Alternative materials based on double perovskites<sup>12-15</sup> and low-dimensional perovskites<sup>15-20</sup> are also being explored as they enrich the structural diversity and property repertoire of the perovskite framework. The 3D perovskite structure which forms by the corner-sharing motif of the  $\text{MX}_6$  octahedra of  $\text{Pb}^{2+}$  and  $\text{Sn}^{2+}$  creates a favorable electronic band structure with very broad valence and conduction bands which facilitate photo-excited charge transport.<sup>21-22</sup> It is this type of electronic band structure, along with the special lattice dynamics, that underpin the very promising optoelectronic properties of the perovskites. Theoretical DFT calculations of various metal halide structures show that the electronic band dispersions are larger in the corner-sharing motifs than in edge-sharing ones, while the face-sharing structures have relatively flat bands and poor charge transport.<sup>23-25</sup> This raises the interesting question: is it possible to find structure motifs for Pb and Sn based hybrids beyond the perovskite paradigm that can still exhibit comparable electronic properties for practical applications? Currently, we cannot fully answer the question because the scope of non-perovskite halide hybrids with Pb and Sn is relatively limited.

The 3D perovskite structure has defined cages which are stabilized by the so called Goldschmidt tolerance factor,<sup>26</sup> a geometrical constraint that must be met by the A cations in the general formula  $\text{AMX}_3$  ( $\text{M} = \text{Ge}^{2+}$ ,  $\text{Sn}^{2+}$ ,  $\text{Pb}^{2+}$ ;  $\text{X} = \text{Cl}^-$ ,  $\text{Br}^-$ ,  $\text{I}^-$ ).<sup>5-6</sup> So far, only three +1 A-site cations can maintain the 3D structures:  $\text{Cs}^+$ ,  $\text{CH}_3\text{NH}_3^+$  (MA), or  $\text{HC}(\text{NH}_2)_2^+$  (FA). When the A cation is as big as ethylenediammonium (en), it can replace some of the  $\text{M}^{2+}$  forming the “hollow” perovskites with decreasing mass densities as the amount of en increases,<sup>27-28</sup>. When it comes to  $\text{HOC}_2\text{H}_4\text{NH}_3^+$  (hea) cation<sup>29-30</sup>, some  $\text{Pb}^{2+}$  and  $\text{I}^-$  deficient channels are formed with the  $\text{Pb}^{2+}$  and  $\text{I}^-$  ions partially replaced by the hea cation, and as a result, the volume of the unit cell is larger than that of the  $\text{MAPbI}_3$ . For cations with three or more carbons, two-dimensional (2D)<sup>25, 31-32</sup> and one-dimensional (1D) structures<sup>33</sup> are formed to accommodate them.<sup>34</sup> For example, the linear diammonium cations  $\text{NH}_3\text{C}_m\text{H}_{2m}\text{NH}_3^{2+}$  ( $m = 4-9$ ) lead to the 2D  $(\text{NH}_3\text{C}_m\text{H}_{2m}\text{NH}_3)(\text{CH}_3\text{NH}_3)_{n-1}\text{Pb}_n\text{I}_{3n+1}$  ( $m = 4-9$ ,  $n = 1-4$ ) series.<sup>35</sup> The cyclic diammonium cations x-(aminomethyl)piperidium (xAMP,  $x = 3$  or  $4$ ) template the Dion-Jacobson phases  $(\text{xAMP})(\text{CH}_3\text{NH}_3)_{n-1}\text{Pb}_n\text{I}_{3n+1}$  ( $n = 1-4$ ).<sup>36</sup> As in the case of x-aminomethylpyridium (AMPY) ( $x =$

1  
2  
3 2, 3 or 4) cations, they form 2D, 0D and 1D structures with 2AMPY, 3AMPY and 4AMPY for  
4 bromide compounds, respectively.<sup>37</sup> For iodide compounds, 2AMPY cation can form either 1D  
5 structure that incorporate crystalline H<sub>2</sub>O in the lattice or 2D structures that preclude H<sub>2</sub>O, and  
6 these structures can be converted below 90 °C.<sup>38-39</sup> Recently, our group reported that 3AMPY and  
7 4AMPY cations can also template multilayered 2D Dion-Jacobson phases (xAMPY)(MA)<sub>n</sub>-  
8 <sub>1</sub>Pb<sub>n</sub>I<sub>3n+1</sub> (x = 3 or 4, n = 1-4).<sup>40</sup> In many lower dimensional structures, however, the connectivity  
9 mode is not limited to corner-sharing only, edge-sharing and face-sharing<sup>31</sup> modes are also  
10 commonly seen. These materials are no longer proper perovskites and can be referred to as  
11 “perovskitoids”.<sup>41</sup>

12 Here, we show that the xAMPY cations can stabilize 3D perovskitoid structures with Sn and Pb  
13 that consist of both corner-sharing and edge-sharing octahedra. The compounds have a double  
14 AMX<sub>3</sub> formula, (xAMPY)M<sub>2</sub>I<sub>6</sub>, and theoretical DFT calculations show that their electronic  
15 structures resemble those of the 3D AMX<sub>3</sub> perovskites. The bandgaps of the new compounds are  
16 ~0.5 eV wider than the AMX<sub>3</sub> 3D perovskites because the polyhedron connectivity is a mixture of  
17 corner-sharing and edge-sharing motifs. The bandwidths are large along the directions of corner-  
18 sharing, leading to low carrier effective masses and the bandgaps still fall within the range for solar  
19 cell and X-ray radiation detector applications. Raman spectra reveal a broad response that is  
20 consistent with the loss of translational symmetry with phonons from across the Brillouin zone  
21 apparently contributing to scattering of the incident light, suggesting lattice phonon dynamics  
22 typical of liquids and high anharmonicity. Interestingly, this response is similar to the 3D MAPbX<sub>3</sub>  
23 perovskites whose lattices are dynamical and possess dual “crystal-liquid” characteristics, causing  
24 large polaron formation and good screening of charge carriers. In this context, we show that  
25 (3AMPY)Pb<sub>2</sub>I<sub>6</sub> exhibit promising optical and electronic properties suitable for radiation detector  
26 applications. They exhibit high X-ray sensitivity of 207 μC·Gy<sup>-1</sup>·cm<sup>-2</sup> and robust photoresponse  
27 under ambient light even without applied bias, which can be attributed to its large carrier mobility  
28 and lifetime product.

## 29 30 31 32 33 34 35 36 37 38 39 40 41 42 43 44 45 46 47 48 49 50 **Experimental Section**

51  
52 **Starting Materials** PbI<sub>2</sub> (99.999%), SnCl<sub>2</sub>·2H<sub>2</sub>O (99%), hydroiodic acid (57 wt % in H<sub>2</sub>O,  
53 distilled, stabilized, 99.95%), hypophosphorous acid solution (50 wt % in H<sub>2</sub>O), 3-  
54  
55  
56  
57  
58  
59  
60

(aminomethyl)pyridine (99%) and 4-(aminomethyl)pyridine (98%) were purchased from Sigma-Aldrich and used as received.

### Synthesis.

*(3AMPY)Pb<sub>2</sub>I<sub>6</sub>* An amount of 2 mmol (446.4 mg) PbO was dissolved in 2.5 mL concentrated HI solution under heating to boiling and vigorous stirring until a clear yellow solution was obtained. 0.5 mmol (50.8  $\mu$ L) 3-(aminomethyl)pyridine (3AMPY) was added to 0.5 mL hypophosphorous acid in a separate vial under stirring. The protonated 3AMPY solution was added to the previous solution under continuous heating at 240 °C and stirred for 5 min. Then the temperature was lowered to 125 °C until red crystals precipitated out. After one hour most crystals had precipitated out, the product was isolated by suction filtration from the hot solution and dried on the filtration funnel for a further 30 min. Yield: 375 mg, 22.7% based on total Pb.

*(4AMPY)Pb<sub>2</sub>I<sub>6</sub>* An amount of 2 mmol (446.4 mg) PbO was dissolved in 2.5 mL concentrated HI solution under heating to boiling and vigorous stirring until a clear yellow solution was obtained. 0.4 mmol (40.6  $\mu$ L) 4-(aminomethyl)pyridine (4AMPY) was added to 0.5 mL hypophosphorous acid in a separate vial under stirring. The protonated 4AMPY solution was added to the previous solution under continuous heating at 240 °C and stirred for 5 min. Then the temperature was lowered to 125 °C until orange crystals precipitated out. After one hour most crystals had precipitated out, the product was isolated by suction filtration from the hot solution and dried on the filtration funnel for a further 30 min. Yield: 281.3 mg, 17.1% based on total Pb.

*(3AMPY)Sn<sub>2</sub>I<sub>6</sub>* An amount of 2 mmol (451.3 mg) SnCl<sub>2</sub>·2H<sub>2</sub>O was dissolved in 2.5 mL concentrated HI solution under heating to boiling and vigorous stirring until a clear yellow solution was obtained. 0.5 mmol (50.8  $\mu$ L) 3AMPY was added to 0.5 mL hypophosphorous acid in a separate vial under stirring. The protonated 3AMPY solution was added to the previous solution under continuous heating at 240 °C and stirred for 5 min. Then the temperature was lowered to 125 °C until black crystals precipitated out. After one hour most crystals had precipitated out, the product was isolated by suction filtration from the hot solution and dried on the filtration funnel for a further 30 min. Yield: 268.1 mg, 24.2% based on total Sn.

*(4AMPY)Sn<sub>2</sub>I<sub>6</sub>* An amount of 2 mmol (451.3 mg) SnCl<sub>2</sub>·2H<sub>2</sub>O was dissolved in 2.5 mL concentrated HI solution under heating to boiling and vigorous stirring until a clear yellow solution was obtained. 0.5 mmol (50.8  $\mu$ L) 4AMPY was added to 0.5 mL hypophosphorous acid in a separate vial under stirring. The protonated 3AMPY solution was added to the previous solution

1  
2  
3 under continuous heating at 240 °C and stirred for 5 min. Then the temperature was lowered to  
4 125 °C until dark red crystals precipitated out. After one hour most crystals precipitated out, the  
5 product was isolated by suction filtration from the hot solution and dried on the filtration funnel  
6 for a further 30 min. Yield: 231.2 mg, 20.8% based on total Sn.  
7  
8

9  
10 *(3AMPY)<sub>1-x</sub>(4AMPY)<sub>x</sub>Sn<sub>2</sub>I<sub>6</sub>* An amount of 2 mmol (451.3 mg) SnCl<sub>2</sub>·2H<sub>2</sub>O was dissolved in 2.5  
11 mL concentrated HI solution under heating to boiling and vigorous stirring until a clear yellow  
12 solution was obtained. 0.5(1-x) mmol 3AMPY and 0.5x mmol 4AMPY (x = 0.25, 0.5, 0.75) were  
13 added to 0.5 mL hypophosphorous acid in a separate vial under stirring. The protonated solution  
14 was added to the previous solution under continuous heating at 240 °C and stirred for 5 min. Then  
15 the temperature was lowered to 125 °C until black crystals precipitated out. After one hour most  
16 crystals precipitated out, the product was isolated by suction filtration from the hot solution and  
17 dried on the filtration funnel for a further 30 min.  
18

19  
20 *(3AMPY)(Pb<sub>1-x</sub>Sn<sub>x</sub>)<sub>2</sub>I<sub>6</sub>* An amount of 2x mmol SnCl<sub>2</sub>·2H<sub>2</sub>O and 2(1-x) mmol PbO (x = 0.25, 0.5,  
21 0.75) were dissolved in 2.5 mL concentrated HI solution under heating to boiling and vigorous  
22 stirring until a clear yellow solution was obtained. 0.5 mmol (50.8 μL) 3AMPY was added to 0.5  
23 mL hypophosphorous acid in a separate vial under stirring. The protonated 3AMPY solution was  
24 added to the previous solution under continuous heating at 240 °C and stirred for 5 min. Then the  
25 temperature was lowered to 125 °C until black crystals precipitated out. After one hour most  
26 crystals had precipitated out, the product was isolated by suction filtration from the hot solution  
27 and dried on the filtration funnel for a further 30 min.  
28

29  
30 **Single Crystal Structure.** Single-crystal X-ray diffraction experiments were performed using a  
31 STOE IPDS II or IPDS 2T diffractometer with Mo K $\alpha$  radiation ( $\lambda = 0.71073$  Å) and operating at  
32 50 kV and 40 mA. Integration and numerical absorption corrections were performed using the X-  
33 AREA, X-RED, and XSHAPE programs. The structures were solved by charge flipping and  
34 refined by full-matrix least-squares on F<sup>2</sup> using the Jana 2006 package.<sup>42</sup> The PLATON<sup>43</sup> software  
35 was used to identify the twinning domains and validate the space groups of the compounds.  
36

37  
38 **Computational details.** First-principles calculations are based on density functional theory (DFT)  
39 as implemented in the SIESTA package.<sup>44-45</sup> Calculations have been carried out on experimental  
40 structures with the GGA functional in the revPBE form.<sup>46</sup> Core electrons are described with  
41 Troullier-Martins pseudopotentials,<sup>47</sup> while valence wavefunctions are developed over double- $\zeta$   
42 polarized basis set of finite-range numerical pseudoatomic orbitals.<sup>48</sup> In our calculations, spin-orbit  
43  
44  
45  
46  
47  
48  
49  
50  
51  
52  
53  
54  
55  
56  
57

1  
2  
3 coupling is taken into account through the on-site approximation as proposed by Fernández-  
4 Seivane et al.<sup>49</sup> In all cases, an energy cutoff of 150 Ry for real-space mesh size has been used.

5  
6 **Detector Fabrication and Performance Measurements.** The (3AMPY)Pb<sub>2</sub>I<sub>6</sub> crystal was used to  
7 fabricate the detector with the structure of Ga/(3AMPY)Pb<sub>2</sub>I<sub>6</sub>/Au. Au electrodes were prepared by  
8 conductive adhesive paint. Ga electrode was prepared by spreading liquid Ga metal on the surface.  
9  
10 The I – V curves were measured using a Keithley 6517B electrometer. The photoconductivity  
11 measurement was done under ambient light under AM1.5 G simulated irradiation with a standard  
12 solar simulator (Abet Technologies) with a flux of 10 mW/cm<sup>2</sup>. The X-ray response was measured  
13 using an uncollimated X-ray source, generated by Amptek Ag Mini X-ray tube with the operation  
14 tube voltage of 50 kV. During measurement, the X-ray beam was filtered by Al pad for reducing  
15 the dose rate. The dose rate was tuned by changing the tube current from 10 to 60 μA.  
16  
17  
18  
19  
20  
21  
22  
23  
24

## 25 **Results and Discussion**

26  
27 **Synthesis.** To avoid the previously reported 2D perovskite (xAMPY)PbI<sub>4</sub> structures, which  
28 formed when the ratio of Pb and AMPY starting materials is 1:1,<sup>40</sup> we used a 4:1 ratio which led  
29 to the new compounds. After all reactants dissolved under stirring and boiling, if the solution was  
30 cooled directly to the room temperature, the compounds could not form, and instead light-yellow  
31 phases precipitated out. These are hydrated phases formed, which were also observed as  
32 intermediates in the synthesis of the 2D (xAMPY)PbI<sub>4</sub> structures.<sup>40</sup> Similar orange hydrated phases  
33 were also observed for the Sn analogues. Therefore, to avoid these light-yellow phases, the hot  
34 plate temperature needs to be lowered from 240°C to 125°C (right below the boiling point of HI)  
35 to keep the solution hot and prevent their precipitation. It is worth mentioning that the solution  
36 temperature cannot exceed the boiling point of concentrated HI (~127 °C) which is a “physical  
37 constant” for the given concentration of solutes. The excess heat produced by the 240 °C  
38 temperature on the hot plate is only relevant in assessing the rate of the solvent evaporation rather  
39 than the actual temperature of the reaction and was chosen to accelerate the synthetic process. The  
40 solutions need to be very concentrated so that the desired phase can still precipitate out at 125°C.  
41 Plate-like crystals started to form from the hot 125°C solution within one hour, and the crystal  
42 growth process was completed within one more hour. The formed crystals were filtered by suction  
43 filtration directly from the hot solution to avoid the formation of the hydrated phases. The color of  
44  
45  
46  
47  
48  
49  
50  
51  
52  
53  
54  
55  
56  
57  
58  
59  
60



1  
2  
3 the (3AMPY)Pb<sub>2</sub>I<sub>6</sub> crystal is red while that of (4AMPY)Pb<sub>2</sub>I<sub>6</sub> is orange. The colors of  
4 (3AMPY)Sn<sub>2</sub>I<sub>6</sub> and (4AMPY)Sn<sub>2</sub>I<sub>6</sub>, are black and dark red, respectively, and all the crystals are  
5 plate-like in shape. The pictures of the crystals are shown as insets in Figure S1, and the  
6 experimental power X-ray diffraction (PXRD) patterns match the calculated ones, showing that  
7 pure phases are obtained during the synthesis. Both Sn compounds have the same crystal structure  
8 as (3AMPY)Pb<sub>2</sub>I<sub>6</sub>, which makes mixing both A<sup>+</sup> and M<sup>2+</sup> cations to form isostructural alloys  
9 possible. The mixed A<sup>+</sup> cation compounds exhibit a continuous color change between  
10 (3AMPY)Sn<sub>2</sub>I<sub>6</sub> and (4AMPY)Sn<sub>2</sub>I<sub>6</sub>. For the mixed Pb/Sn compounds, all crystals are black as their  
11 optical bandgaps are smaller than both parent compounds (see below).

12  
13  
14  
15  
16  
17  
18  
19 **Crystal structures.** The general formula of the new materials is (xAMPY)M<sub>2</sub>I<sub>6</sub>, (x = 3 or 4, M =  
20 Pb<sup>2+</sup> or Sn<sup>2+</sup>), which is equivalent to a doubled 3D perovskite AMI<sub>3</sub> formula where two A<sup>+</sup> cations  
21 are substituted by a single +2 xAMPY cation. However, the large xAMPY cations template  
22 different structures with a combination of corner-sharing and edge-sharing octahedra, giving rise  
23 to two unique metal-halide frameworks. All compounds crystallize in the polar monoclinic space  
24 groups *Ia/Im*, with the results of structural refinement shown in Table 1, and detailed  
25 crystallographic data provided in Tables S1–S5. It is worth mentioning that the inorganic  
26 structures are noncentrosymmetric locally (i.e. in a single unit cell), but in the long-range bulk they  
27 tend to be centrosymmetric as the dipoles cancel out on average. This picture is in line with the  
28 dynamic crystal structure of the halide perovskites (especially at room temperature) which makes  
29 such an equivocal structural interpretation possible (see detailed discussion of the Raman spectra  
30 below). We chose the noncentrosymmetric space groups to avoid the disorder in the model as we  
31 have explained in detail for 2D structure refinements previously.<sup>50</sup> (3AMPY)Sn<sub>2</sub>I<sub>6</sub> and  
32 (4AMPY)Sn<sub>2</sub>I<sub>6</sub> adopt the same space group as (3AMPY)Pb<sub>2</sub>I<sub>6</sub> (*Im*), whereas the (4AMPY)Pb<sub>2</sub>I<sub>6</sub>  
33 compound exhibits a different space group (*Ia*). Therefore, the two types of structures will be  
34 discussed separately. The unit cells in both cases consist of four layers of octahedra, summing up  
35 to a lattice parameter of ~25 Å, which represents a 4-fold supercell of the basic octahedral motif  
36 (4×~6.3 Å).

37  
38  
39  
40  
41  
42  
43  
44  
45  
46  
47  
48  
49  
50  
51 **Crystal structure of (4AMPY)Pb<sub>2</sub>I<sub>6</sub>.** There are four crystallographically independent Pb atoms  
52 forming four distinct octahedra in the (4AMPY)Pb<sub>2</sub>I<sub>6</sub> structure (Figure 1a), and two of them are  
53 connected by edge-sharing to form dimers, which then further connect through corner-sharing to  
54  
55  
56  
57

1  
2  
3 other dimers to form continuous layers extending along the *bc* crystallographic plane. Four edge-  
4 sharing dimers connect through corners across the individual layers to form triangular-shaped  
5 voids (Figure 2a, 2b). The layers then stack by corner-connect along the *a*-axis (stacking axis) to  
6 complete the anionic inorganic 3D framework (Figure 2c). The characteristic size and shape of the  
7 4AMPY act as a template, forming a large isosceles triangle-shaped cavity around which the  
8 network structure is built. The 4AMPY cation lies in the plane of the layers and perpendicular to  
9 the stacking direction in the channels, a configuration that is imposed by the charge density  
10 distribution of the organic atoms. Although all layers are the same, they stack in pairs. This is  
11 shown by the yellow and purple layers in Figure 2a-c. Within a pair the layers stack in an eclipsed  
12 manner. Between pairs the stacking is accomplished by a  $1/2 \times 1/2$  shift along the *b* and *c* axes,  
13 Figure 2d. The two adjacent bilayers between pairs are symmetry-related by glide planes. Viewed  
14 along the *a*-axis, the lattice contains rhombus-shaped channels (Figure 2d).

24 **Crystal structure of (3AMPY) $M_2I_6$  ( $M = Pb^{2+}$  or  $Sn^{2+}$ ).** The structure of (3AMPY) $Pb_2I_6$  consists  
25 of six distinct Pb atoms (Figure 1b), and the basic motif is also dimers formed by two edge-sharing  
26 octahedra of adjacent Pb atoms. Its structure is different from that of (4AMPY) $Pb_2I_6$  in the  
27 interconnectivity of the edge-sharing dimers. In this case there are two chemically distinct types  
28 of layers. The first kind consists of corner-sharing merging from four dimer to form rectangular  
29 cavities instead of triangles (Figure 3a, c), and they are symmetry-related by a mirror plane. The  
30 second kind is the same as the one described above in the (4AMPY) $Pb_2I_6$  structure with triangular  
31 cavities (Figure 3b, d). The structure of (3AMPY) $Pb_2I_6$  can be thought as stacking of these layers  
32 in an alternating fashion along the *b* direction, Figures 3e. The triangular and rectangular voids  
33 containing the organic cations interchange across the stacking *b* axis every other layer, Figure 3f.  
34  
35  
36  
37  
38  
39  
40  
41

42 The Sn analogues crystallize in the (3AMPY) $Pb_2I_6$  structure type. Similar to the (3AMPY) $Pb_2I_6$   
43 structure, each of the four layers in the unit cell adopt a different connection motif, as shown in  
44 Figure 3a-d. Figure 4 shows the structures from a side view and the connection motif for the bottom  
45 layer. The difference in distortion between (3AMPY) $Sn_2I_6$  and (4AMPY) $Sn_2I_6$  can be seen from  
46 the close inspection of the bottom layer of the two structures. Specifically, the shape of the cage is  
47 a regular rectangle for (3AMPY) $Sn_2I_6$ , Figure 4b, whereas for (4AMPY) $Sn_2I_6$  the rectangle is  
48 significantly deformed, Figure 4d.  
49  
50  
51  
52  
53  
54  
55  
56  
57  
58  
59  
60

Because of the strong links to the electronic properties, it is important to analyze the connectivity types of the metal iodide octahedra in these structures as well as the M-I-M angles and bonding distortions. To simplify the discussion, we only consider the M-I-M angles of corner-sharing connectivity, since they are the special feature in perovskites and most relevant to the charge transport and electronic band dispersion. The M-I-M angles can be divided into the “equatorial” M-I-M angles which are perpendicular to the stacking axis and the “axial” M-I-M angles that align parallel to the stacking axis, Table 2. For the Pb compounds, the (4AMPY)Pb<sub>2</sub>I<sub>6</sub> structure has smaller equatorial angles than (3AMPY)Pb<sub>2</sub>I<sub>6</sub> because the Pb-I-Pb acute angles of the triangular cavity are much smaller than 180°. The (3AMPY)Pb<sub>2</sub>I<sub>6</sub> structure has half the number of triangular cavity and half rectangular cavity, where the Pb-I-Pb angles for the rectangular cavity are almost 180°. Therefore, the (3AMPY)Pb<sub>2</sub>I<sub>6</sub> structure has on average larger equatorial Pb-I-Pb angles than the (4AMPY)Pb<sub>2</sub>I<sub>6</sub> structure. For the Sn compounds, even though the connection motif is the same, the Sn-I-Sn angles are different, as seen from the large deformation of the rectangular cavity (Figure 4d). The (3AMPY)Sn<sub>2</sub>I<sub>6</sub> structure has larger equatorial and axial Sn-I-Sn angles, so the average Sn-I-Sn angles are also larger than the (4AMPY)Sn<sub>2</sub>I<sub>6</sub> structure, Table 2.

We can also compare the average distortion levels of individual octahedra. This structural distortion can be quantified by defining the distortion index (D) and bond angle variance ( $\sigma^2$ ) of the octahedra by the variance of the M-I bond-length and M-I-M bond-angle from the average value calculated by the Vesta software,<sup>51-52</sup> as shown in equation (1) and (2), where  $l_{av}$  is the average M-I bond distance,  $l_i$  are the individual bond-length and  $\phi_i$  is the individual bond-angle. For the structures with multiple independent octahedra, the average values are used. The distortion index and bond angle variance are significantly higher in the (4AMPY)Sn<sub>2</sub>I<sub>6</sub> than those in the (3AMPY)Sn<sub>2</sub>I<sub>6</sub> (Table 2), and the values for (3AMPY)<sub>0.5</sub>(4AMPY)<sub>0.5</sub>Sn<sub>2</sub>I<sub>6</sub> are between the two parent compounds. The structures of the Pb compounds are less distorted and the corresponding the D and  $\sigma^2$  values are shown in Table 2.

$$D = \frac{1}{6} \sum_i \frac{6|l_i - l_{av}|}{l_{av}} \quad (1)$$

$$\sigma^2 = \sum_{i=1}^{12} (\phi_i - 90)^2 / 11 \quad (2)$$

The similarity of structures between (3AMPY)Pb<sub>2</sub>I<sub>6</sub> and (3AMPY)Sn<sub>2</sub>I<sub>6</sub> makes it possible to mix the M<sup>2+</sup> cations to form the (3AMPY)(Pb<sub>1-x</sub>Sn<sub>x</sub>)<sub>2</sub>I<sub>6</sub> series with  $x = 0.25, 0.5$  and  $0.75$ . The structure

of (3AMPY)PbSnI<sub>6</sub> ( $x = 0.5$ ) adopts the same space group as the two parent compounds, and the unit cell dimensions lie in between (3AMPY)Pb<sub>2</sub>I<sub>6</sub> and (3AMPY)Sn<sub>2</sub>I<sub>6</sub> (as shown Table 1). For  $x = 0.5$ , the actual ratio of Sn and Pb is obtained by refining the occupancy of the M<sup>2+</sup> site, with 1.09 Sn: 0.91Pb close to the stoichiometric reaction ratio (1:1).

**Electronic structure calculations.** We calculated the electronic band structures using DFT with the experimentally obtained structures. Note that in the case of 3AMPY and 4AMPY organic cations, the well-known bandgap underestimation of GGA functionals causes the artificial appearance of molecular states from the organic cation within the band of the inorganic lattice. This is caused by the incorrect positions of the conduction and valence band extrema with respect to the lowest unoccupied molecular orbital (LUMO) of the organic cations. In order to circumvent this artifact, we performed calculations by substituting the organic cations with an estimated background charge. This way, the misplaced molecular cation states no longer appear in the band structure, while the band structure arising from the inorganic lattice is not dramatically affected (Figure S2a, b). All four compounds ( $x$ AMPY)M<sub>2</sub>I<sub>6</sub> ( $x = 3$  or  $4$ , M = Sn<sup>2+</sup> or Pb<sup>2+</sup>) are indirect bandgap semiconductors. For the Sn compounds, the valence band maxima (VBM) show up at the A point while the conduction band minima (CBM) are at the  $\Gamma$  point (Figure 5a, b). The calculated bandgaps of the indirect transition are 0.81 eV and 0.80 eV for the (3AMPY)Sn<sub>2</sub>I<sub>6</sub> and (4AMPY)Sn<sub>2</sub>I<sub>6</sub>, respectively.

Despite the indirect bandgap, which may account for the weak photoluminescence (PL) at room temperature (see below), there is a closely lying, slightly larger direct bandgap at the  $\Gamma$  point which can account for the significant optical absorption exhibited by these materials. As shown in Figure S2c, the CB and VB wavefunctions display linear combinations of orbitals both at the A and  $\Gamma$  points, which are favorable for direct dipolar electric transitions. The CB edge wavefunctions are indeed based on empty  $p$ -orbitals located on the Pb atoms and the VB edge wavefunctions on combinations of filled  $p$ -orbitals located on the iodine atoms and on filled  $s$ -orbitals located on the Pb atoms. These linear combinations of orbitals are typical of halide perovskites and stand at the origin of their remarkable optoelectronic properties. These strong direct optical transitions are in principle competing with indirect optical transitions between the A and  $\Gamma$ , *i.e.* from the VB (A) to the CB ( $\Gamma$ ) and from the VB ( $\Gamma$ ) to the CB (A), which is in sharp contrast to the conventional indirect semiconductors such as Si, where the direct transition is very weak.<sup>53</sup>

1  
2  
3 The octahedra in the  $b$  direction (for the Sn compound) are connected in corner-sharing mode,  
4 while in the other two directions there is a combination of corner-sharing and edge-sharing.  
5 Therefore, the  $\Gamma Y$  (MA) direction in the Brillouin zone, which corresponds to the  $b$  direction in  
6 the real space, is the most energy dispersive direction for both VB and CB. This is in marked  
7 contrast to the other crystallographic directions where the octahedra share edges and the associated  
8 electronic bands are much less dispersive. This is consistent with our understanding that the corner-  
9 sharing motif results in larger band dispersions than the edge-sharing one, followed by the face-  
10 sharing motif.<sup>23-25</sup>

11  
12 The Pb compounds have relatively flat valence bands and dispersive conduction bands. The VBM  
13 show up at the Y point while the CBM at the  $\Gamma$  point. The (3AMPY)Pb<sub>2</sub>I<sub>6</sub> and (4AMPY)Pb<sub>2</sub>I<sub>6</sub>  
14 compounds exhibit larger calculated bandgaps than the Sn analogs at 1.41 eV and 1.44 eV (Figure  
15 5c, d), which match the experimental trend. The (4AMPY)Pb<sub>2</sub>I<sub>6</sub> shows strong differences from  
16 the other three compounds, with the VBM and CBM showing up in different positions in the  
17 Brillouin zone, which reflects its different crystallographic structure.

18  
19 It is notable that the VBM and CBM of the Pb compounds are much less dispersive than the Sn  
20 analogs and this is also reflected in the computed carrier effective masses that are at least two times  
21 higher for Pb (Table 3). The strong spin-orbit coupling (SOC) pushes the filled 6s based bands of  
22 the Pb perovskites lower in energy compared to the 5s bands of the Sn perovskites, decreasing  
23 their contribution to the VBM.<sup>54</sup> The significant energy stabilization of the 6s based bands of the  
24 Pb perovskites result in narrowing of the valence bands. This trend, also observed in the 3D  
25 perovskites, suggests that the Sn compounds should have overall better hole and electron  
26 mobilities.<sup>21</sup> In the case of Sn perovskites, however, a strong anisotropy appears when looking  
27 closely at hole and electron effective masses. Indeed, the carrier effective masses in the corner-  
28 sharing direction ( $m_h^{\parallel}$  and  $m_e^{\parallel}$ ) are significantly smaller than the masses taken perpendicular to  
29 that direction ( $m_h^{\perp}$  and  $m_e^{\perp}$ , see Table 3). The contrast is greater for electrons with a ratio  $m_e^{\parallel}/m_e^{\perp}$   
30 larger than 20 for 3AMPY and 4AMPY, but is also strong for holes with a ratio  $m_h^{\parallel}/m_h^{\perp}$  greater  
31 than 10 and 3.5 for 3AMPY and 4AMPY, respectively. This indicates that the Sn compounds are  
32 considerably more anisotropic in an electronic transport sense despite the 3D structure of the  
33 framework. The anisotropy also exists for Pb compounds but is less pronounced, in particular for  
34 holes with  $m_h^{\parallel}/m_h^{\perp}$  ratios lesser than 2. These results call for a careful orientation of the  
35  
36  
37  
38  
39  
40  
41  
42  
43  
44  
45  
46  
47  
48  
49  
50  
51  
52  
53  
54  
55  
56  
57  
58  
59  
60

1  
2  
3 compounds within a device for full utilization of the charge mobilities. Given the energy dispersive  
4 nature of the conduction bands of the Pb compounds, the  $m_e$  is favorably small and suggests good  
5 electron transport properties.  
6  
7

8  
9 **Raman Spectra.** The room-temperature Raman spectra of the compounds, shown in Figure 6,  
10 consist of very broad, low intensity peaks. displaying similar behavior to the conventional 3D  
11  $AMX_3$  structures. The spectra are diffuse, composed of a central peak with a notable spectral  
12 continuum from very broad Raman transitions. For the Pb compounds, the peaks at lower  
13 frequencies ( $<70\text{ cm}^{-1}$ ) correspond to the bending modes of  $[PbI_6]^{4-}$  octahedra while the peak at  
14  $\sim 100\text{ cm}^{-1}$  corresponds to the  $[PbI_6]^{4-}$  stretching modes.<sup>55</sup> The Raman spectra for the Sn compounds  
15 are even more diffuse, with one broad peak expanding the measurement range. The broad central  
16 peak located around  $0\text{ cm}^{-1}$  betrays loss of translational symmetry and is characteristic of dynamic  
17 atomic disorder, highly anharmonic, and dissipative vibrations.<sup>56-57</sup> This type of room temperature  
18 Raman spectrum has been observed in crystalline  $MAPbI_3$ ,  $MAPbBr_3$  and  $CsPbBr_3$  perovskites  
19 which are known to have soft distortive lattices and interestingly similar to those of fluids.<sup>55, 58</sup> In  
20 essence the broad central peaks suggests one can view these anharmonic crystalline structures as  
21 vibrating in almost all frequencies. This behavior is attributed to local polar fluctuations and high  
22 anharmonicity that derive from the  $6s^2$  ( $5s^2$ ) lone pair activity of  $Pb^{2+}$  ( $Sn^{2+}$ ) and halide motion.  
23 These fluctuations are intrinsic to the general metal-halide perovskite structure and the presence  
24 of corner-sharing octahedra and less so to any dipolar organic cation.<sup>54</sup> This fluid-like behavior in  
25 the inorganic lattice is believed to cause the beneficial defect tolerant properties of 3D perovskites  
26 and implies that the title  $(3AMPY)(Pb_{1-x}Sn_x)_2I_6$  and  $(4AMPY)(Pb_{1-x}Sn_x)_2I_6$  compounds also  
27 possess similar characteristics considering the large fraction of corner-sharing octahedra.  
28  
29  
30  
31  
32  
33  
34  
35  
36  
37  
38  
39  
40  
41

42 **Optoelectronic properties.** The absorption spectra of the four parent compounds are shown in  
43 Figure S3, and the absorption spectra of the  $(3AMPY)(Pb_{1-x}Sn_x)_2I_6$  series are presented in Figure  
44 7a. An optical feature near the optical band gap similar to an excitonic resonance is prominent only  
45 for the pure Pb compound. We may infer that an excitonic resonance can be barely seen in the Sn  
46 or the mixed Sn/Pb compounds, indicating lower excitonic binding energies for the Sn-based  
47 perovskites.<sup>59-60</sup> The bandgap values (Figure 7b, d) were extracted from the low-energy slope of  
48 the Tauc plot (Figure S4). As suggested above by the electronic structure calculations, the  
49 compounds are technically indirect bandgap semiconductors but practically seem to behave as  
50  
51  
52  
53  
54  
55  
56  
57  
58  
59  
60

1  
2  
3 direct bandgap materials. This can explain the experimental results that some of the absorption  
4 spectra (especially those of mixed AMPY cations, shown in Figure 7c) have a low energy tail  
5 (likely indicative of structural disorder) and the PL intensities are low (compared to perovskite  
6 compounds) at room temperature (Figure S3b, d). Though the estimated bandgaps are slightly  
7 different when the Tauc plots are drawn based on the indirect (Figure S4) and direct bandgap  
8 models (Figure S5), the trend is the same among the compounds.  
9

14 As it is typical in halide perovskites, the Sn compounds exhibit smaller bandgap than the Pb ones.  
15 The intermediate mixed Pb/Sn compounds, however, show anomalous trend and exhibit smaller  
16 bandgaps than the parent Sn and Pb compounds. This trend, called the bowing effect, defies the  
17 so-called Vegard's law and comes from the fact that the Sn compound has deeper conduction band  
18 minimum (CBM) and the Pb compound has shallower valence band maximum (VBM) with respect  
19 to each other.<sup>61-62</sup> Because of this trend, most alloy combinations of Sn and Pb will generate lower  
20 bandgaps than the Sn compounds.<sup>63-64</sup> As for the mixed cation (3AMPY)<sub>1-x</sub>(4AMPY)<sub>x</sub>Sn<sub>2</sub>I<sub>6</sub> series,  
21 the bandgaps of the intermediate compounds do fall between the two parent ones following  
22 Vegard's law. The bandgaps enlarge as the fraction of 4AMPY increases, even though the trend is  
23 not perfectly linear.  
24  
25  
26  
27  
28  
29  
30

31  
32 In 2D perovskites, the bandgaps are related to the distortion level defined by the M-I-M angles.<sup>65</sup>  
33 As discussed previously, we simplify the structure by only looking at the corner-sharing M-I-M  
34 angles (Table 2). In the present case, the average Pb-I-Pb angles for the (3AMPY)Pb<sub>2</sub>I<sub>6</sub> structure  
35 are larger because of the coexistence of the triangular and rectangular cavities, while for the  
36 (4AMPY)Pb<sub>2</sub>I<sub>6</sub> structure, there are only triangular cavities with acute Pb-I-Pb angles (Table 2).  
37 Therefore, for the (3AMPY)Pb<sub>2</sub>I<sub>6</sub> structure the Pb s- and I p-orbitals have better overlap in the  
38 direction of charge transport, resulting in a smaller bandgaps. For both the Sn compounds, even  
39 though the connection motif is the same, the (4AMPY)Sn<sub>2</sub>I<sub>6</sub> structure has deformed rectangular  
40 cavities (because of more distorted SnI<sub>6</sub> octahedra) and smaller Sn-I-Sn angles, and thus a larger  
41 bandgap than the (3AMPY)Sn<sub>2</sub>I<sub>6</sub> structure.  
42  
43  
44  
45  
46  
47  
48  
49

50 Even though the M-I-M angles play a major role in determining the bandgap, we can also compare  
51 the local distortion of individual octahedra by looking at the distortion index (D), as defined above,  
52 to gain further insight on structure-property relationships. The structures with higher bandgaps  
53 tend to have larger local distortions. For example, D is larger for (4AMPY)Sn<sub>2</sub>I<sub>6</sub>, so  
54  
55  
56  
57

(4AMPY)Sn<sub>2</sub>I<sub>6</sub> has a higher bandgap than (3AMPY)Sn<sub>2</sub>I<sub>6</sub> (Table 2). The D of the mixed 3AMPY/4AMPY compound falls between the two parent ones and so does the bandgap. But for structures with different connection motif, such as (3AMPY)Pb<sub>2</sub>I<sub>6</sub> and (4AMPY)Pb<sub>2</sub>I<sub>6</sub>, it is still the Pb-I-Pb angles that mainly determine the bandgap.

### Photoresponse

Based on the promising optical and electronic properties of these materials, we carried out a preliminary assessment of the photoresponse by selecting crystals of the (3AMPY)Pb<sub>2</sub>I<sub>6</sub> compound. Gallium and gold electrodes were applied on the *ab* plane with the electric field along the *b* direction, where all the octahedra are connected by corner-sharing. The (3AMPY)Pb<sub>2</sub>I<sub>6</sub> exhibits a high electrical resistivity of 6×10<sup>8</sup> Ω cm (Figure S6a), similar to MAPbI<sub>3</sub>.<sup>11, 66</sup> When exposed to ambient light, the device based on the Ga/(3AMPY)Pb<sub>2</sub>I<sub>6</sub>/Au structure showed a clear photoresponse (Figure S6a). Because of the Schottky barrier formed by the work function difference of Ga and Au, the device exhibits reversible on-off switching property under ambient light even without an external field (Figure S6b). The on-off photoresponse was also measured under 2V bias resulting in higher photocurrent (Figure 8a). Photoconductivity measurements on the device carried out under a 10 mW/cm<sup>2</sup> lamp indicate a pronounced photoresponse with a 10 times higher photocurrent than the dark current (Figure 8b). These results suggest great potential for photo detection applications at room temperature.

Because of the high density (4.06 g/cm<sup>3</sup>) and the presence of heavy Pb element, the (3AMPY)Pb<sub>2</sub>I<sub>6</sub> has a high X-ray absorption coefficient and a prominent X-ray detection response. Figure 8c shows the X-ray photocurrent of the (3AMPY)Pb<sub>2</sub>I<sub>6</sub> device using the uncollimated Ag X-ray tube with a dose rate of 259.1 μGy/s and a peak voltage of 50 kV. The product of charge carrier mobility ( $\mu$ ) and carrier lifetime ( $\tau$ ) is a figure of merit used to evaluate the effectiveness of X-ray radiation detectors and can be obtained from the I-V data using the Many equation<sup>67-68</sup> (eq (3)), where  $I_0$  is the saturated photocurrent,  $V$  is the applied bias and  $L$  is the thickness.

$$I = \frac{I_0 \mu \tau V [1 - \exp(-\frac{L^2}{\mu \tau V})]}{L^2 \left(1 + \frac{Ls}{V\mu}\right)} \quad (3)$$

The fitting in Figure 8c for the (3AMPY)Pb<sub>2</sub>I<sub>6</sub> device yields a  $\mu\tau$  product of 1.2×10<sup>-4</sup> cm<sup>2</sup>/V, which is similar to the value reported for MAPbI<sub>3</sub>.<sup>11</sup> This is an impressive  $\mu\tau$  value and shows a promising



charge collection performance for X-ray detection applications. The X-ray sensitivity was also determined by measuring the X-ray response under different radiation dose rates (Figure S7). The X-ray dose was controlled by varying the Ag X-ray tube current from 10  $\mu\text{A}$  to 60  $\mu\text{A}$  and was measured by a dosimeter. The photocurrent density of the (3AMPY) $\text{Pb}_2\text{I}_6$  device increases with X-ray dose rate and follows a linear relationship which is consistent with a well behaved semiconductor (Figure 8d). The extracted X-ray sensitivity of the device is high at 207  $\mu\text{C}\cdot\text{Gy}^{-1}\cdot\text{cm}^{-2}$ . This value is comparable to the state-of-art commercialized materials  $\text{Cd}_{1-x}\text{Zn}_x\text{Te}$  (CZT) (318  $\mu\text{C}\cdot\text{Gy}^{-1}\cdot\text{cm}^{-2}$ ) and  $\alpha\text{-Se}$  (20  $\mu\text{C}\cdot\text{Gy}^{-1}\cdot\text{cm}^{-2}$ ).<sup>69</sup> Here, we only report preliminary results of X-ray detection as we believe the material can achieve better performance after optimization of crystal quality, size, device structure and controlled orientation within a device for full utilization of the charge mobilities.

## Conclusions

The organic di-cations xAMPY (x=3, 4) template two new types of 3D halide networks in (xAMPY) $\text{Sn}_2\text{I}_6$  and (xAMPY) $\text{Pb}_2\text{I}_6$ . Their structures feature a combination of corner-sharing and edge-sharing octahedra. Because of the multiple modes of linking of the  $\text{MI}_6$  octahedra, these compounds are not proper perovskites and belong to the broader class of so-called perovskitoids. The bandgaps of the Sn and Pb compounds are  $\sim 1.7$  eV and  $\sim 2.0$  eV, respectively. DFT calculations indicate that these compounds are indirect bandgap semiconductors but with additional direct bandgaps at slightly higher energies and band structures that resemble those of the  $\text{AMI}_3$  perovskites. The band structures are anisotropic and exhibit large electronic band dispersions and low effective electron masses, especially along the direction in which all octahedra are corner-shared, with the Sn analogs having broader bands. The lattices seem to undergo local polar fluctuations with crystal-liquid lattice dynamics as suggested by the Raman scattering experiments. This is expected to result in large polaron formation in these materials and good screening of charge carriers, leading to defect tolerance, similar to 3D perovskites. Indeed, these special characteristics and the favorable electronic structure of the compounds lead to large photoresponse under ambient light even without an applied bias. (3AMPY) $\text{Pb}_2\text{I}_6$  crystals also show excellent response under Ag X-ray irradiation, with a high carrier mobility and lifetime product ( $\mu\tau$ ) of  $1.2\times 10^{-4}$   $\text{cm}^2/\text{V}$  and an X-ray sensitivity of 207  $\mu\text{C}\cdot\text{Gy}^{-1}\cdot\text{cm}^{-2}$ .

## Associated Content

### Supporting information

Additional experimental details for powder X-ray diffraction, absorption spectroscopy, Raman spectroscopy, crystallographic details, experimental and calculated PXRD patterns, and optoelectronic properties.

X-ray crystallographic data of (3AMPY)Pb<sub>2</sub>I<sub>6</sub>.

X-ray crystallographic data of (4AMPY)Pb<sub>2</sub>I<sub>6</sub>.

X-ray crystallographic data of (3AMPY)Sn<sub>2</sub>I<sub>6</sub>.

X-ray crystallographic data of (4AMPY)Sn<sub>2</sub>I<sub>6</sub>.

X-ray crystallographic data of (3AMPY)PbSnI<sub>6</sub>.

X-ray crystallographic data of (3AMPY)<sub>0.5</sub>(4AMPY)<sub>0.5</sub>Sn<sub>2</sub>I<sub>6</sub>.

### Author information

#### Corresponding Author

[\\*m-kanatzidis@northwestern.edu](mailto:m-kanatzidis@northwestern.edu)

### Notes

The authors declare no competing financial interest.

### Acknowledgements

At Northwestern University this work is mainly supported by the Department of Energy, Office of Science, Basic Energy Sciences, under Grant No. SC0012541 (synthesis, structure, and physical property characterization). DFT calculations were performed at the Institut des Sciences Chimiques de Rennes, which received funding from the Agence Nationale pour la Recherche (TRANSHYPERO project) and the work was granted access to the HPC resources of TGCC/CINES/IDRIS under the allocation 2018-A0010907682 made by GENCI. M. K. acknowledges support from Region Bretagne through Boost'ERC LaHPerOS project. J.E acknowledges the financial support from the Institut Universitaire de France. Raman measurements were performed at GeoSoilEnviroCARS (The University of Chicago, Sector 13), Advanced Photon Source (APS), Argonne National Laboratory. GeoSoilEnviroCARS is supported by the National Science Foundation - Earth Sciences (EAR - 1634415). The Raman system

1  
2  
3 acquisition was supported by the NSF MRI proposal (EAR-1531583). This work was performed,  
4 in part, at the Center for Nanoscale Materials, a U.S. Department of Energy Office of Science User  
5 Facility, and supported by the U.S. Department of Energy, Office of Science, under Contract No.  
6 DE-AC02-06CH11357. This work made use of the SPID (confocal microscopy) facilities of  
7 Northwestern University's NUANCE Center, which has received support from the Soft and Hybrid  
8 Nanotechnology Experimental Resource (NSF ECCS1542205), the Materials Research Science  
9 and Engineering Centers (NSF DMR-1720139), the International Institute for Nanotechnology  
10 (IIN), the Keck Foundation, and the State of Illinois through the IIN.  
11  
12  
13  
14  
15  
16  
17  
18  
19  
20  
21  
22  
23  
24  
25  
26  
27  
28  
29  
30  
31  
32  
33  
34  
35  
36  
37  
38  
39  
40  
41  
42  
43  
44  
45  
46  
47  
48  
49  
50  
51  
52  
53  
54  
55  
56  
57  
58  
59  
60

## References

1. Tsai, H.; Asadpour, R.; Blancon, J.-C.; Stoumpos, C. C.; Durand, O.; Strzalka, J. W.; Chen, B.; Verduzco, R.; Ajayan, P. M.; Tretiak, S.; Even, J.; Alam, M. A.; Kanatzidis, M. G.; Nie, W.; Mohite, A. D., Light-induced lattice expansion leads to high-efficiency perovskite solar cells. *Science* **2018**, *360* (6384), 67-70.
2. Yang, W. S.; Park, B.-W.; Jung, E. H.; Jeon, N. J.; Kim, Y. C.; Lee, D. U.; Shin, S. S.; Seo, J.; Kim, E. K.; Noh, J. H.; Seok, S. I., Iodide management in formamidinium-lead-halide-based perovskite layers for efficient solar cells. *Science* **2017**, *356* (6345), 1376-1379.
3. Arora, N.; Dar, M. I.; Hinderhofer, A.; Pellet, N.; Schreiber, F.; Zakeeruddin, S. M.; Grätzel, M., Perovskite solar cells with CuSCN hole extraction layers yield stabilized efficiencies greater than 20%. *Science* **2017**, *358* (6364), 768-771.
4. Dong, Q.; Fang, Y.; Shao, Y.; Mulligan, P.; Qiu, J.; Cao, L.; Huang, J., Electron-hole diffusion lengths >175  $\mu\text{m}$  in solution-grown  $\text{CH}_3\text{NH}_3\text{PbI}_3$  single crystals. *Science* **2015**, *347* (6225), 967-970.
5. Stoumpos, C. C.; Kanatzidis, M. G., The Renaissance of Halide Perovskites and Their Evolution as Emerging Semiconductors. *Acc. Chem. Res.* **2015**, *48* (10), 2791-2802.
6. Stoumpos, C. C.; Kanatzidis, M. G., Halide Perovskites: Poor Man's High-Performance Semiconductors. *Adv. Mater.* **2016**, *28* (28), 5778-5793.
7. Fang, Y.; Dong, Q.; Shao, Y.; Yuan, Y.; Huang, J., Highly narrowband perovskite single-crystal photodetectors enabled by surface-charge recombination. *Nat. Photonics* **2015**, *9*, 679.
8. Wei, H.; Fang, Y.; Mulligan, P.; Chuirazzi, W.; Fang, H.-H.; Wang, C.; Ecker, B. R.; Gao, Y.; Loi, M. A.; Cao, L.; Huang, J., Sensitive X-ray detectors made of methylammonium lead tribromide perovskite single crystals. *Nat. Photonics* **2016**, *10*, 333.
9. Wei, H.; DeSantis, D.; Wei, W.; Deng, Y.; Guo, D.; Savenije, T. J.; Cao, L.; Huang, J., Dopant compensation in alloyed  $\text{CH}_3\text{NH}_3\text{PbBr}_{3-x}\text{Cl}_x$  perovskite single crystals for gamma-ray spectroscopy. *Nat. Mater.* **2017**, *16*, 826.
10. He, Y.; Matei, L.; Jung, H. J.; McCall, K. M.; Chen, M.; Stoumpos, C. C.; Liu, Z.; Peters, J. A.; Chung, D. Y.; Wessels, B. W.; Wasielewski, M. R.; Dravid, V. P.; Burger, A.; Kanatzidis, M. G., High spectral resolution of gamma-rays at room temperature by perovskite  $\text{CsPbBr}_3$  single crystals. *Nat. Commun.* **2018**, *9* (1), 1609.
11. He, Y.; Ke, W.; Alexander, G. C. B.; McCall, K. M.; Chica, D. G.; Liu, Z.; Hadar, I.; Stoumpos, C. C.; Wessels, B. W.; Kanatzidis, M. G., Resolving the Energy of  $\gamma$ -Ray Photons with  $\text{MAPbI}_3$  Single Crystals. *ACS Photonics* **2018**, *5* (10), 4132-4138.
12. Pan, W.; Wu, H.; Luo, J.; Deng, Z.; Ge, C.; Chen, C.; Jiang, X.; Yin, W.-J.; Niu, G.; Zhu, L.; Yin, L.; Zhou, Y.; Xie, Q.; Ke, X.; Sui, M.; Tang, J.,  $\text{Cs}_2\text{AgBiBr}_6$  single-crystal X-ray detectors with a low detection limit. *Nat. Photonics* **2017**, *11* (11), 726-732.
13. Yin, L.; Wu, H.; Pan, W.; Yang, B.; Li, P.; Luo, J.; Niu, G.; Tang, J., Controlled Cooling for Synthesis of  $\text{Cs}_2\text{AgBiBr}_6$  Single Crystals and Its Application for X-Ray Detection. *Advanced Optical Materials* **2019**, *7* (19), 1900491.
14. Yang, B.; Pan, W.; Wu, H.; Niu, G.; Yuan, J.-H.; Xue, K.-H.; Yin, L.; Du, X.; Miao, X.-S.; Yang, X.; Xie, Q.; Tang, J., Heteroepitaxial passivation of  $\text{Cs}_2\text{AgBiBr}_6$  wafers with suppressed ionic migration for X-ray imaging. *Nat. Commun.* **2019**, *10* (1), 1989.
15. Xu, Z.; Liu, X.; Li, Y.; Liu, X.; Yang, T.; Ji, C.; Han, S.; Xu, Y.; Luo, J.; Sun, Z., Exploring Lead-Free Hybrid Double Perovskite Crystals of  $(\text{BA})_2\text{CsAgBiBr}_7$  with Large Mobility-Lifetime Product toward X-Ray Detection. *Angew. Chem., Int. Ed.* **2019**, *58* (44), 15757-15761.

16. Zhuang, R.; Wang, X.; Ma, W.; Wu, Y.; Chen, X.; Tang, L.; Zhu, H.; Liu, J.; Wu, L.; Zhou, W.; Liu, X.; Yang, Y., Highly sensitive X-ray detector made of layered perovskite-like  $(\text{NH}_4)_3\text{Bi}_2\text{I}_9$  single crystal with anisotropic response. *Nat. Photonics* **2019**, *13* (9), 602-608.
17. Liu, Y.; Zhang, Y.; Yang, Z.; Ye, H.; Feng, J.; Xu, Z.; Zhang, X.; Munir, R.; Liu, J.; Zuo, P.; Li, Q.; Hu, M.; Meng, L.; Wang, K.; Smilgies, D.-M.; Zhao, G.; Xu, H.; Yang, Z.; Amassian, A.; Li, J.; Zhao, K.; Liu, S., Multi-inch single-crystalline perovskite membrane for high-detectivity flexible photosensors. *Nat. Commun.* **2018**, *9* (1), 5302.
18. Sun, Q.; Xu, Y.; Zhang, H.; Xiao, B.; Liu, X.; Dong, J.; Cheng, Y.; Zhang, B.; Jie, W.; Kanatzidis, M. G., Optical and electronic anisotropies in perovskitoid crystals of  $\text{Cs}_3\text{Bi}_2\text{I}_9$  studies of nuclear radiation detection. *J. Mater. Chem. A* **2018**, *6* (46), 23388-23395.
19. Wang, J.; Li, J.; Lan, S.; Fang, C.; Shen, H.; Xiong, Q.; Li, D., Controllable Growth of Centimeter-Sized 2D Perovskite Heterostructures for Highly Narrow Dual-Band Photodetectors. *ACS Nano* **2019**, *13* (5), 5473-5484.
20. Ji, C.; Wang, S.; Wang, Y.; Chen, H.; Li, L.; Sun, Z.; Sui, Y.; Wang, S.; Luo, J., 2D Hybrid Perovskite Ferroelectric Enables Highly Sensitive X-Ray Detection with Low Driving Voltage. *Adv. Funct. Mater.* **2019**, *n/a* (n/a), 1905529.
21. Umari, P.; Mosconi, E.; De Angelis, F., Relativistic GW calculations on  $\text{CH}_3\text{NH}_3\text{PbI}_3$  and  $\text{CH}_3\text{NH}_3\text{SnI}_3$  Perovskites for Solar Cell Applications. *Sci. Rep.* **2014**, *4*, 4467.
22. Even, J.; Pedesseau, L.; Katan, C., Analysis of Multivalley and Multibandgap Absorption and Enhancement of Free Carriers Related to Exciton Screening in Hybrid Perovskites. *J. Phys. Chem. C* **2014**, *118* (22), 11566-11572.
23. Kamminga, M. E.; de Wijs, G. A.; Havenith, R. W. A.; Blake, G. R.; Palstra, T. T. M., The Role of Connectivity on Electronic Properties of Lead Iodide Perovskite-Derived Compounds. *Inorg. Chem.* **2017**, *56* (14), 8408-8414.
24. Mao, L.; Guo, P.; Kepenekian, M.; Hadar, I.; Katan, C.; Even, J.; Schaller, R. D.; Stoumpos, C. C.; Kanatzidis, M. G., Structural Diversity in White-Light-Emitting Hybrid Lead Bromide Perovskites. *J. Am. Chem. Soc.* **2018**, *140* (40), 13078-13088.
25. Hoffman, J. M.; Che, X.; Sidhik, S.; Li, X.; Hadar, I.; Blancon, J.-C.; Yamaguchi, H.; Kepenekian, M.; Katan, C.; Even, J.; Stoumpos, C. C.; Mohite, A. D.; Kanatzidis, M. G., From 2D to 1D Electronic Dimensionality in Halide Perovskites with Stepped and Flat Layers Using Propylammonium as a Spacer. *J. Am. Chem. Soc.* **2019**, *141* (27), 10661-10676.
26. Kieslich, G.; Sun, S.; Cheetham, A. K., Solid-state principles applied to organic-inorganic perovskites: new tricks for an old dog. *Chem. Sci.* **2014**, *5* (12), 4712-4715.
27. Ke, W.; Stoumpos, C. C.; Zhu, M.; Mao, L.; Spanopoulos, I.; Liu, J.; Kontsevoi, O. Y.; Chen, M.; Sarma, D.; Zhang, Y.; Wasielewski, M. R.; Kanatzidis, M. G., Enhanced photovoltaic performance and stability with a new type of hollow 3D perovskite  $(\text{en})\text{FASnI}_3$ . *Sci. Adv.* **2017**, *3* (8), e1701293.
28. Spanopoulos, I.; Ke, W.; Stoumpos, C. C.; Schueller, E. C.; Kontsevoi, O. Y.; Seshadri, R.; Kanatzidis, M. G., Unraveling the Chemical Nature of the 3D “Hollow” Hybrid Halide Perovskites. *J. Am. Chem. Soc.* **2018**, *140* (17), 5728-5742.
29. Leblanc, A.; Mercier, N.; Allain, M.; Dittmer, J.; Pauporté, T.; Fernandez, V.; Boucher, F.; Kepenekian, M.; Katan, C., Enhanced Stability and Band Gap Tuning of  $\alpha$ - $[\text{HC}(\text{NH}_2)_2]\text{PbI}_3$  Hybrid Perovskite by Large Cation Integration. *ACS Appl. Mater. Interfaces* **2019**, *11* (23), 20743-20751.

- 1  
2  
3 30. Leblanc, A.; Mercier, N.; Allain, M.; Dittmer, J.; Fernandez, V.; Pauporté, T., Lead- and  
4 Iodide-Deficient (CH<sub>3</sub>NH<sub>3</sub>)PbI<sub>3</sub> (d-MAPI): The Bridge between 2D and 3D Hybrid Perovskites.  
5 *Angew. Chem., Int. Ed.* **2017**, *56* (50), 16067-16072.
- 6 31. Mao, L.; Stoumpos, C. C.; Kanatzidis, M. G., Two-Dimensional Hybrid Halide Perovskites:  
7 Principles and Promises. *J. Am. Chem. Soc.* **2019**, *141* (3), 1171-1190.
- 8 32. Li, X.; Guo, P.; Kepenekian, M.; Hadar, I.; Katan, C.; Even, J.; Stoumpos, C. C.; Schaller,  
9 R. D.; Kanatzidis, M. G., Small Cyclic Diammonium Cation Templated (110)-Oriented 2D Halide  
10 (X = I, Br, Cl) Perovskites with White-Light Emission. *Chem. Mater.* **2019**, *31* (9), 3582-3590.
- 11 33. Ben Haj Salah, M.; Mercier, N.; Allain, M.; Zouari, N.; Botta, C., Dual phosphorescence  
12 from the organic and inorganic moieties of 1D hybrid perovskites of the Pb<sub>n</sub>Br<sub>4n'+2</sub> series (n' = 2,  
13 3, 4, 5). *J. Mater. Chem. C* **2019**, *7* (15), 4424-4433.
- 14 34. Katan, C.; Mercier, N.; Even, J., Quantum and Dielectric Confinement Effects in Lower-  
15 Dimensional Hybrid Perovskite Semiconductors. *Chem. Rev.* **2019**, *119* (5), 3140-3192.
- 16 35. Li, X.; Hoffman, J.; Ke, W.; Chen, M.; Tsai, H.; Nie, W.; Mohite, A. D.; Kepenekian, M.;  
17 Katan, C.; Even, J.; Wasielewski, M. R.; Stoumpos, C. C.; Kanatzidis, M. G., Two-Dimensional  
18 Halide Perovskites Incorporating Straight Chain Symmetric Diammonium Ions,  
19 (NH<sub>3</sub>C<sub>m</sub>H<sub>2m</sub>NH<sub>3</sub>)(CH<sub>3</sub>NH<sub>3</sub>)<sub>n-1</sub>Pb<sub>n</sub>I<sub>3n+1</sub> (m = 4–9; n = 1–4). *J. Am. Chem. Soc.* **2018**, *140* (38),  
20 12226-12238.
- 21 36. Mao, L.; Ke, W.; Pedesseau, L.; Wu, Y.; Katan, C.; Even, J.; Wasielewski, M. R.;  
22 Stoumpos, C. C.; Kanatzidis, M. G., Hybrid Dion–Jacobson 2D Lead Iodide Perovskites. *J. Am.*  
23 *Chem. Soc.* **2018**, *140* (10), 3775-3783.
- 24 37. Li, Y.; Zheng, G.; Lin, C.; Lin, J., Synthesis, structure and optical properties of different  
25 dimensional organic–inorganic perovskites. *Solid State Sci.* **2007**, *9* (9), 855-861.
- 26 38. Yu, H.; Wei, Z.; Hao, Y.; Liang, Z.; Fu, Z.; Cai, H., Reversible solid-state thermochromism  
27 of a 2D organic–inorganic hybrid perovskite structure based on iodoplumbate and 2-aminomethyl-  
28 pyridine. *New J. Chem.* **2017**, *41* (18), 9586-9589.
- 29 39. Lermer, C.; Senocrate, A.; Moudrakovski, I.; Seewald, T.; Hatz, A.-K.; Mayer, P.;  
30 Pielnhofer, F.; Jaser, J. A.; Schmidt-Mende, L.; Maier, J.; Lotsch, B. V., Completing the Picture  
31 of 2-(Aminomethylpyridinium) Lead Hybrid Perovskites: Insights into Structure, Conductivity  
32 Behavior, and Optical Properties. *Chem. Mater.* **2018**, *30* (18), 6289-6297.
- 33 40. Li, X.; Ke, W.; Traoré, B.; Guo, P.; Hadar, I.; Kepenekian, M.; Even, J.; Katan, C.;  
34 Stoumpos, C. C.; Schaller, R. D.; Kanatzidis, M. G., Two-Dimensional Dion–Jacobson Hybrid  
35 Lead Iodide Perovskites with Aromatic Diammonium Cations. *J. Am. Chem. Soc.* **2019**, *141* (32),  
36 12880-12890.
- 37 41. Stoumpos, C. C.; Mao, L.; Malliakas, C. D.; Kanatzidis, M. G., Structure–Band Gap  
38 Relationships in Hexagonal Polytypes and Low-Dimensional Structures of Hybrid Tin Iodide  
39 Perovskites. *Inorg. Chem.* **2017**, *56* (1), 56-73.
- 40 42. Petříček, V.; Dušek, M.; Palatinus, L., Crystallographic Computing System JANA2006:  
41 General features. *Z. Kristallogr. - Cryst. Mater.* **2014**, *229* (5), 345.
- 42 43. Spek, A., Structure validation in chemical crystallography. *Acta Crystallogr. D* **2009**, *65*  
43 (2), 148-155.
- 44 44. Artacho, E.; Anglada, E.; Diéguez, O.; Gale, J. D.; García, A.; Junquera, J.; Martin, R. M.;  
45 Ordejón, P.; Pruneda, J. M.; Sánchez-Portal, D.; Soler, J. M., The SIESTA method; developments  
46 and applicability. *J. Phys.: Condens. Matter* **2008**, *20* (6), 064208.
- 47  
48  
49  
50  
51  
52  
53  
54  
55  
56  
57  
58  
59  
60

- 1  
2  
3 45. Soler, J. M.; Artacho, E.; Gale, J. D.; García, A.; Junquera, J.; Ordejón, P.; Sánchez-Portal,  
4 D., The SIESTA method for ab initio order- N materials simulation. *J. Phys.: Condens. Matter*  
5 **2002**, *14* (11), 2745.
- 6 46. Zhang, Y.; Yang, W., Comment on "Generalized Gradient Approximation Made Simple".  
7 *Phys. Rev. Lett.* **1998**, *80* (4), 890-890.
- 8 47. Troullier, N.; Martins, J. L., Efficient pseudopotentials for plane-wave calculations. *Phys.*  
9 *Rev. B* **1991**, *43* (3), 1993-2006.
- 10 48. Artacho, E.; Sánchez-Portal, D.; Ordejón, P.; García, A.; Soler, J. M., Linear-Scaling ab-  
11 initio Calculations for Large and Complex Systems. *Phys. Status Solidi B* **1999**, *215* (1), 809-817.
- 12 49. Fernández-Seivane, L.; Oliveira, M. A.; Sanvito, S.; Ferrer, J., On-site approximation for  
13 spin-orbit coupling in linear combination of atomic orbitals density functional methods. *J. Phys.:*  
14 *Condens. Matter* **2006**, *18* (34), 7999.
- 15 50. Stoumpos, C. C.; Cao, D. H.; Clark, D. J.; Young, J.; Rondinelli, J. M.; Jang, J. I.; Hupp,  
16 J. T.; Kanatzidis, M. G., Ruddlesden-Popper Hybrid Lead Iodide Perovskite 2D Homologous  
17 Semiconductors. *Chem. Mater.* **2016**, *28* (8), 2852-2867.
- 18 51. Robinson, K.; Gibbs, G. V.; Ribbe, P. H., Quadratic Elongation: A Quantitative Measure  
19 of Distortion in Coordination Polyhedra. *Science* **1971**, *172* (3983), 567-570.
- 20 52. Momma, K.; Izumi, F., VESTA 3 for three-dimensional visualization of crystal, volumetric  
21 and morphology data. *J. Appl. Cryst.* **2011**, *44* (6), 1272-1276.
- 22 53. Chelikowsky, J.; Chadi, D. J.; Cohen, M. L., Calculated Valence-Band Densities of States  
23 and Photoemission Spectra of Diamond and Zinc-Blende Semiconductors. *Phys. Rev. B* **1973**, *8*  
24 (6), 2786-2794.
- 25 54. Fabini, D. H.; Laurita, G.; Bechtel, J. S.; Stoumpos, C. C.; Evans, H. A.; Kontos, A. G.;  
26 Raptis, Y. S.; Falaras, P.; Van der Ven, A.; Kanatzidis, M. G.; Seshadri, R., Dynamic  
27 Stereochemical Activity of the Sn<sup>2+</sup> Lone Pair in Perovskite CsSnBr<sub>3</sub>. *J. Am. Chem. Soc.* **2016**,  
28 *138* (36), 11820-11832.
- 29 55. Quarti, C.; Grancini, G.; Mosconi, E.; Bruno, P.; Ball, J. M.; Lee, M. M.; Snaith, H. J.;  
30 Petrozza, A.; De Angelis, F., The Raman Spectrum of the CH<sub>3</sub>NH<sub>3</sub>PbI<sub>3</sub> Hybrid Perovskite:  
31 Interplay of Theory and Experiment. *J. Phys. Chem. Lett.* **2014**, *5* (2), 279-284.
- 32 56. Zhu, H.; Miyata, K.; Fu, Y.; Wang, J.; Joshi, P. P.; Niesner, D.; Williams, K. W.; Jin, S.;  
33 Zhu, X.-Y., Screening in crystalline liquids protects energetic carriers in hybrid perovskites.  
34 *Science* **2016**, *353* (6306), 1409-1413.
- 35 57. Miyata, K.; Atallah, T. L.; Zhu, X.-Y., Lead halide perovskites: Crystal-liquid duality,  
36 phonon glass electron crystals, and large polaron formation. *Sci. Adv.* **2017**, *3* (10), e1701469.
- 37 58. Yaffe, O.; Guo, Y.; Tan, L. Z.; Egger, D. A.; Hull, T.; Stoumpos, C. C.; Zheng, F.; Heinz,  
38 T. F.; Kronik, L.; Kanatzidis, M. G.; Owen, J. S.; Rappe, A. M.; Pimenta, M. A.; Brus, L. E., Local  
39 Polar Fluctuations in Lead Halide Perovskite Crystals. *Phys. Rev. Lett.* **2017**, *118* (13), 136001.
- 40 59. Huang, L.-y.; Lambrecht, W. R. L., Electronic band structure, phonons, and exciton  
41 binding energies of halide perovskites CsSnCl<sub>3</sub>, CsSnBr<sub>3</sub>, and CsSnI<sub>3</sub>. *Phys. Rev. B* **2013**, *88* (16),  
42 165203.
- 43 60. Cao, D. H.; Stoumpos, C. C.; Yokoyama, T.; Logsdon, J. L.; Song, T.-B.; Farha, O. K.;  
44 Wasielewski, M. R.; Hupp, J. T.; Kanatzidis, M. G., Thin Films and Solar Cells Based on  
45 Semiconducting Two-Dimensional Ruddlesden-Popper (CH<sub>3</sub>(CH<sub>2</sub>)<sub>3</sub>NH<sub>3</sub>)<sub>2</sub>(CH<sub>3</sub>NH<sub>3</sub>)<sub>n-1</sub>Sn<sub>n</sub>I<sub>3n+1</sub>  
46 Perovskites. *ACS Energy Lett.* **2017**, *2* (5), 982-990.
- 47  
48  
49  
50  
51  
52  
53  
54  
55  
56  
57  
58  
59  
60

- 1  
2  
3 61. Wang, C.; Song, Z.; Li, C.; Zhao, D.; Yan, Y., Low-Bandgap Mixed Tin-Lead Perovskites  
4 and Their Applications in All-Perovskite Tandem Solar Cells. *Adv. Funct. Mater.* **2019**, *0* (0),  
5 1808801.  
6  
7 62. Goyal, A.; McKechnie, S.; Pashov, D.; Tumas, W.; van Schilfgaarde, M.; Stevanović, V.,  
8 Origin of Pronounced Nonlinear Band Gap Behavior in Lead–Tin Hybrid Perovskite Alloys. *Chem.*  
9 *Mater.* **2018**, *30* (11), 3920-3928.  
10  
11 63. Hao, F.; Stoumpos, C. C.; Chang, R. P. H.; Kanatzidis, M. G., Anomalous Band Gap  
12 Behavior in Mixed Sn and Pb Perovskites Enables Broadening of Absorption Spectrum in Solar  
13 Cells. *J. Am. Chem. Soc.* **2014**, *136* (22), 8094-8099.  
14  
15 64. Mao, L.; Tsai, H.; Nie, W.; Ma, L.; Im, J.; Stoumpos, C. C.; Malliakas, C. D.; Hao, F.;  
16 Wasielewski, M. R.; Mohite, A. D.; Kanatzidis, M. G., Role of Organic Counterion in Lead- and  
17 Tin-Based Two-Dimensional Semiconducting Iodide Perovskites and Application in Planar Solar  
18 Cells. *Chem. Mater.* **2016**, *28* (21), 7781-7792.  
19  
20 65. Knutson, J. L.; Martin, J. D.; Mitzi, D. B., Tuning the Band Gap in Hybrid Tin Iodide  
21 Perovskite Semiconductors Using Structural Templating. *Inorg. Chem.* **2005**, *44* (13), 4699-4705.  
22  
23 66. Stoumpos, C. C.; Malliakas, C. D.; Kanatzidis, M. G., Semiconducting Tin and Lead Iodide  
24 Perovskites with Organic Cations: Phase Transitions, High Mobilities, and Near-Infrared  
25 Photoluminescent Properties. *Inorg. Chem.* **2013**, *52* (15), 9019-9038.  
26  
27 67. Many, A., High-field effects in photoconducting cadmium sulphide. *J. Phys. Chem. Solids*  
28 **1965**, *26* (3), 575-578.  
29  
30 68. Stoumpos, C. C.; Malliakas, C. D.; Peters, J. A.; Liu, Z.; Sebastian, M.; Im, J.; Chasapis,  
31 T. C.; Wibowo, A. C.; Chung, D. Y.; Freeman, A. J.; Wessels, B. W.; Kanatzidis, M. G., Crystal  
32 Growth of the Perovskite Semiconductor CsPbBr<sub>3</sub>: A New Material for High-Energy Radiation  
33 Detection. *Cryst. Growth Des.* **2013**, *13* (7), 2722-2727.  
34  
35 69. Wei, H.; Huang, J., Halide lead perovskites for ionizing radiation detection. *Nat. Commun.*  
36 **2019**, *10* (1), 1066.  
37  
38  
39  
40  
41  
42  
43  
44  
45  
46  
47  
48  
49  
50  
51  
52  
53  
54  
55  
56  
57  
58  
59  
60



Table 1. Crystal and Refinement Data for Compounds Reported Here

Compound	(3AMPY)Pb <sub>2</sub> I <sub>6</sub>	(3AMPY)PbSnI <sub>6</sub>	(4AMPY)Pb <sub>2</sub> I <sub>6</sub>
Empirical formula	C <sub>6</sub> H <sub>10</sub> I <sub>6</sub> N <sub>2</sub> Pb <sub>2</sub>	C <sub>6</sub> H <sub>10</sub> I <sub>6</sub> N <sub>2</sub> Pb <sub>0.91</sub> Sn <sub>1.09</sub>	C <sub>6</sub> H <sub>10</sub> I <sub>6</sub> N <sub>2</sub> Pb <sub>2</sub>
Crystal system	monoclinic	monoclinic	monoclinic
Space group	<i>Im</i>	<i>Im</i>	<i>Ia</i>
Unit cell dimensions	<i>a</i> = 16.3698(12) Å <i>b</i> = 25.6376(16) Å <i>c</i> = 10.0435(6) Å <i>β</i> = 93.198(6)°	<i>a</i> = 16.3397(12) Å <i>b</i> = 25.5520(16) Å <i>c</i> = 10.0204(6) Å <i>β</i> = 93.130(6)°	<i>a</i> = 25.696(5) Å <i>b</i> = 10.153(2) Å <i>c</i> = 16.283(3) Å <i>β</i> = 90.036°
Volume	4208.5(5) Å <sup>3</sup>	4177.4(5) Å <sup>3</sup>	4248.0(14) Å <sup>3</sup>
Density (calculated)	4.0592 g/cm <sup>3</sup>	3.7827 g/cm <sup>3</sup>	4.0215 g/cm <sup>3</sup>
Index ranges	-19 ≤ <i>h</i> ≤ 22 -35 ≤ <i>k</i> ≤ 35, -13 ≤ <i>l</i> ≤ 13	-22 ≤ <i>h</i> ≤ 22 -34 ≤ <i>k</i> ≤ 34 -13 ≤ <i>l</i> ≤ 13	-34 ≤ <i>h</i> ≤ 35 -13 ≤ <i>k</i> ≤ 13 -22 ≤ <i>l</i> ≤ 22
Independent reflections	7376 [R <sub>int</sub> = 0.0559]	7371 [R <sub>int</sub> = 0.0639]	7292 [R <sub>int</sub> = 0.0481]
Completeness to 25°	99%	99%	99%
Data / restraints / parameters	7376 / 16 / 213	7371 / 16 / 216	7292 / 34 / 196
Goodness-of-fit	3.35	2.87	2.12
Final R indices [I > 2σ(I)]	R <sub>obs</sub> = 0.0542 wR <sub>obs</sub> = 0.0595	R <sub>obs</sub> = 0.0523 wR <sub>obs</sub> = 0.0710	R <sub>obs</sub> = 0.0393 wR <sub>obs</sub> = 0.0401
Largest diff. peak and hole	2.89 and -5.19 e·Å <sup>-3</sup>	2.05 and -3.78 e·Å <sup>-3</sup>	1.57 and -1.07 e·Å <sup>-3</sup>
Compound	(3AMPY)Sn <sub>2</sub> I <sub>6</sub>	(3AMPY) <sub>0.5</sub> (4AMPY) <sub>0.5</sub> Sn <sub>2</sub> I <sub>6</sub>	(4AMPY)Sn <sub>2</sub> I <sub>6</sub>
Empirical formula	C <sub>6</sub> H <sub>10</sub> I <sub>6</sub> N <sub>2</sub> Sn <sub>2</sub>	C <sub>6</sub> H <sub>10</sub> I <sub>6</sub> N <sub>2</sub> Sn <sub>2</sub>	C <sub>6</sub> H <sub>10</sub> I <sub>6</sub> N <sub>2</sub> Sn <sub>2</sub>
Crystal system	monoclinic	monoclinic	monoclinic
Space group	<i>Im</i>	<i>Im</i>	<i>Im</i>
Unit cell dimensions	<i>a</i> = 16.2885(12) Å <i>b</i> = 25.4252(16) Å <i>c</i> = 9.9795(6) Å <i>β</i> = 92.951(6)°	<i>a</i> = 16.3185(12) Å <i>b</i> = 25.4637(16) Å <i>c</i> = 10.0068(6) Å <i>β</i> = 92.490(6)°	<i>a</i> = 16.2208(12) Å <i>b</i> = 25.4537(16) Å <i>c</i> = 10.0307(6) Å <i>β</i> = 91.466(6)°
Volume	4127.4(5) Å <sup>3</sup>	4154.2(5) Å <sup>3</sup>	4140.1(5) Å <sup>3</sup>
Density (calculated)	3.5694 g/cm <sup>3</sup>	3.5464 g/cm <sup>3</sup>	3.5585 g/cm <sup>3</sup>
Index ranges	-22 ≤ <i>h</i> ≤ 19 -34 ≤ <i>k</i> ≤ 34 -13 ≤ <i>l</i> ≤ 13	-22 ≤ <i>h</i> ≤ 22 -34 ≤ <i>k</i> ≤ 34 -13 ≤ <i>l</i> ≤ 13	-19 ≤ <i>h</i> ≤ 22 -34 ≤ <i>k</i> ≤ 34 -13 ≤ <i>l</i> ≤ 13
Independent reflections	7289 [R <sub>int</sub> = 0.0384]	7314 [R <sub>int</sub> = 0.0565]	7285 [R <sub>int</sub> = 0.0406]
Completeness to 25°	100%	99%	99%
Data / restraints / parameters	7289 / 18 / 214	7314 / 16 / 214	7285 / 18 / 213
Goodness-of-fit	1.34	4.34	3.14
Final R indices [I > 2σ(I)]	R <sub>obs</sub> = 0.0339 wR <sub>obs</sub> = 0.0306	R <sub>obs</sub> = 0.0557 wR <sub>obs</sub> = 0.0939	R <sub>obs</sub> = 0.0705 wR <sub>obs</sub> = 0.0688
Largest diff. peak and hole	1.30 and -0.97 e·Å <sup>-3</sup>	2.46 and -3.69 e·Å <sup>-3</sup>	3.60 and -3.58 e·Å <sup>-3</sup>

Table 2. Average Equatorial M-I-M Angle, Average Axial M-I-M Angle, Average M-I-M Angle, Distortion Index (D), Bond Angle Variance ( $\sigma^2$ ) and Bandgap for Compounds Reported Here. (Angles are only associated with the corner-sharing octahedra, and those of the edge-sharing octahedra are not listed)

	(3AMPY)Sn <sub>2</sub> I <sub>6</sub>	(3AMPY) <sub>0.5</sub> (4AMPY) <sub>0.5</sub> Sn <sub>2</sub> I <sub>6</sub>	(4AMPY)Sn <sub>2</sub> I <sub>6</sub>	(3AMPY)Pb <sub>2</sub> I <sub>6</sub>	(4AMPY)Pb <sub>2</sub> I <sub>6</sub>
Average equatorial M-I-M angle (°)	168.09	168.90	165.26	167.27	158.47
Average axial M-I-M angle (°)	172.72	172.25	167.66	171.70	173.40
Average M-I-M angle (°)	169.94	170.24	167.90	169.04	165.93
D	0.0113	0.0114	0.0172	0.0103	0.0096
$\sigma^2$	16.7	18.3	35.5	16.5	9.5
Bandgap (eV)	1.72	1.77	1.79	2.05	2.12

Table 3. Calculated Hole ( $m_h$ ) and Electron ( $m_e$ ) Effective Mass for Compounds Reported Here. ( $m_h^{\parallel}$  and  $m_e^{\parallel}$  represent the hole and electron effective masses parallel to the corner-sharing direction.  $m_h^{\perp}$  and  $m_e^{\perp}$  represent the hole and electron effective masses perpendicular to that direction.  $m_h^{\perp}/m_h^{\parallel}$  and  $m_e^{\perp}/m_e^{\parallel}$  represent the ratio between the two directions.)

	Sn		Pb	
	3AMPY	4AMPY	3AMPY	4AMPY
$m_h(m_0)$	-0.163	-0.154	-0.372	-0.787
$m_e(m_0)$	0.119	0.126	0.251	0.276
$m_h^{\parallel}(m_0)$	-0.035	-0.067	-0.194	-0.535
$m_h^{\perp}(m_0)$	-0.352	-0.234	-0.270	-0.956
$m_h^{\perp}/m_h^{\parallel}$	10.1	3.49	1.39	1.79
$m_e^{\parallel}(m_0)$	0.016	0.017	0.027	0.066
$m_e^{\perp}(m_0)$	0.332	0.344	0.762	0.564
$m_e^{\perp}/m_e^{\parallel}$	20.8	20.2	28.2	8.55

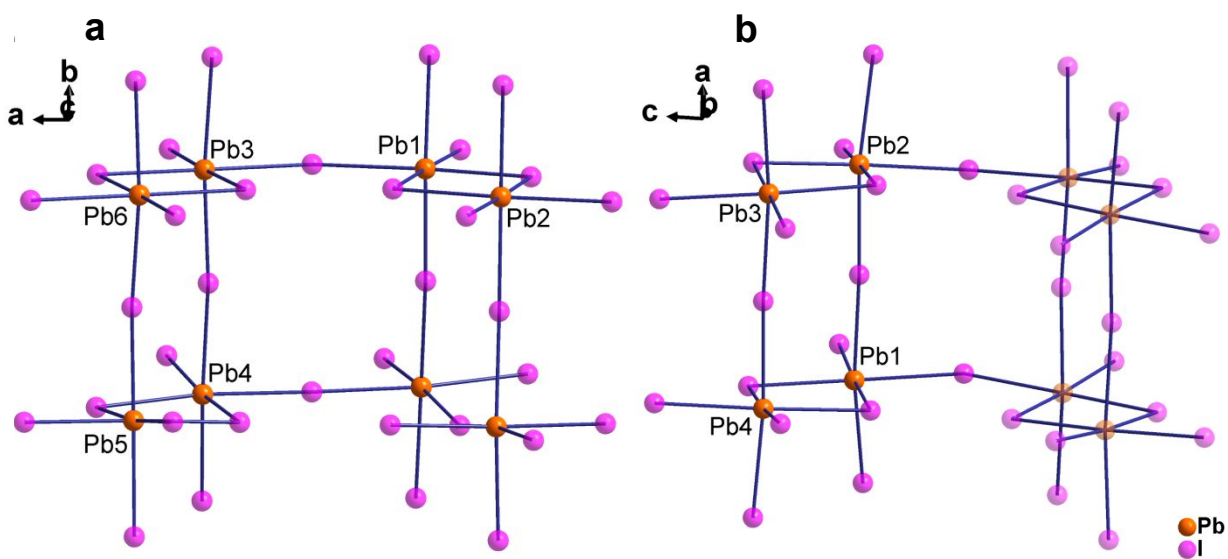


Figure 1. (a) Fragment of  $(4AMPY)Pb_2I_6$  structure. (b) Fragment of  $(3AMPY)Pb_2I_6$  structure showing coordination environment and connectivity of octahedra. The structures feature a combination of linear corner-sharing linkages and bent edge-sharing ones.

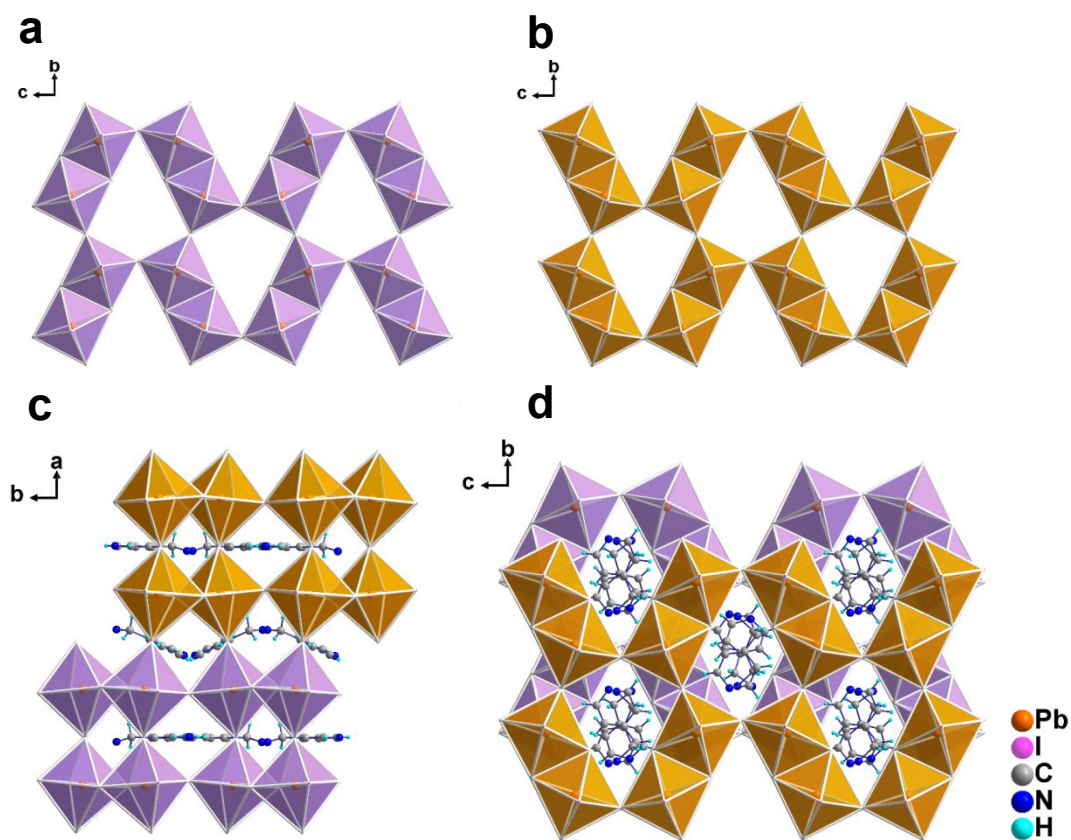


Figure 2. Crystal structures for (4AMPY)Pb<sub>2</sub>I<sub>6</sub>. (a) Connection motif of the octahedra for the bottom two layers. (b) Connection motif for the top two layers. They are symmetry-related by glide planes (organic cations omitted for clarity). (c) Crystal structure from side view. (d) Crystal structure from top view. The colors indicate the layers shown in (a) and (b).

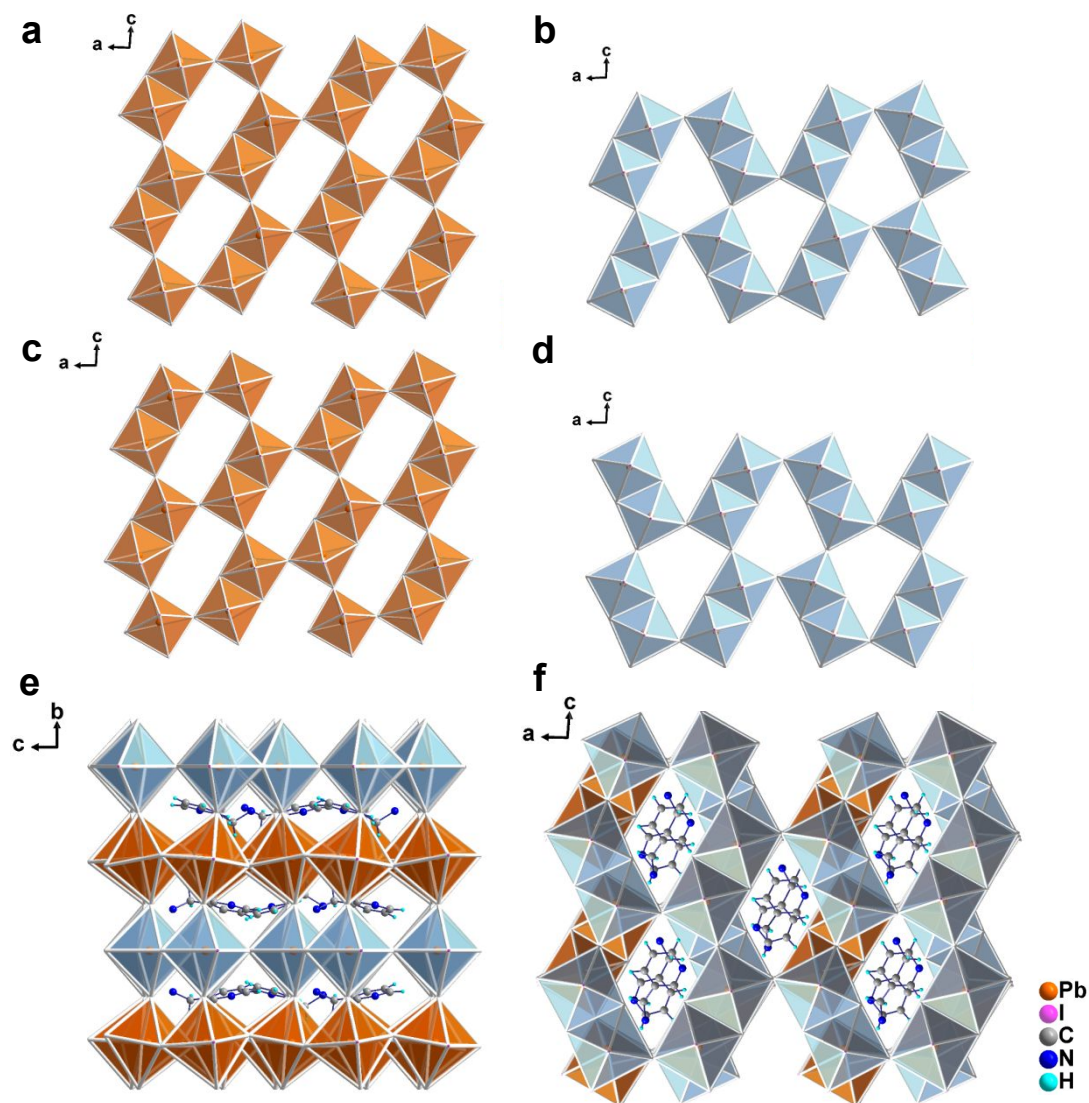


Figure 3. Crystal structure of (3AMPY)Pb<sub>2</sub>I<sub>6</sub>. (a) Connection motif of the octahedra for the bottom layer. (b) Connection motif for the second layer. (c) Connection motif for the third layer. (d) Connection motif for the top layer. The first and third layers are symmetry-related by a mirror plane, and the second and fourth layers are symmetry-related by a glide plane (organic cations omitted for clarity). (e) Crystal structure from side view. (f) Crystal structure from top view. The colors indicate the layers shown in (a)-(d).

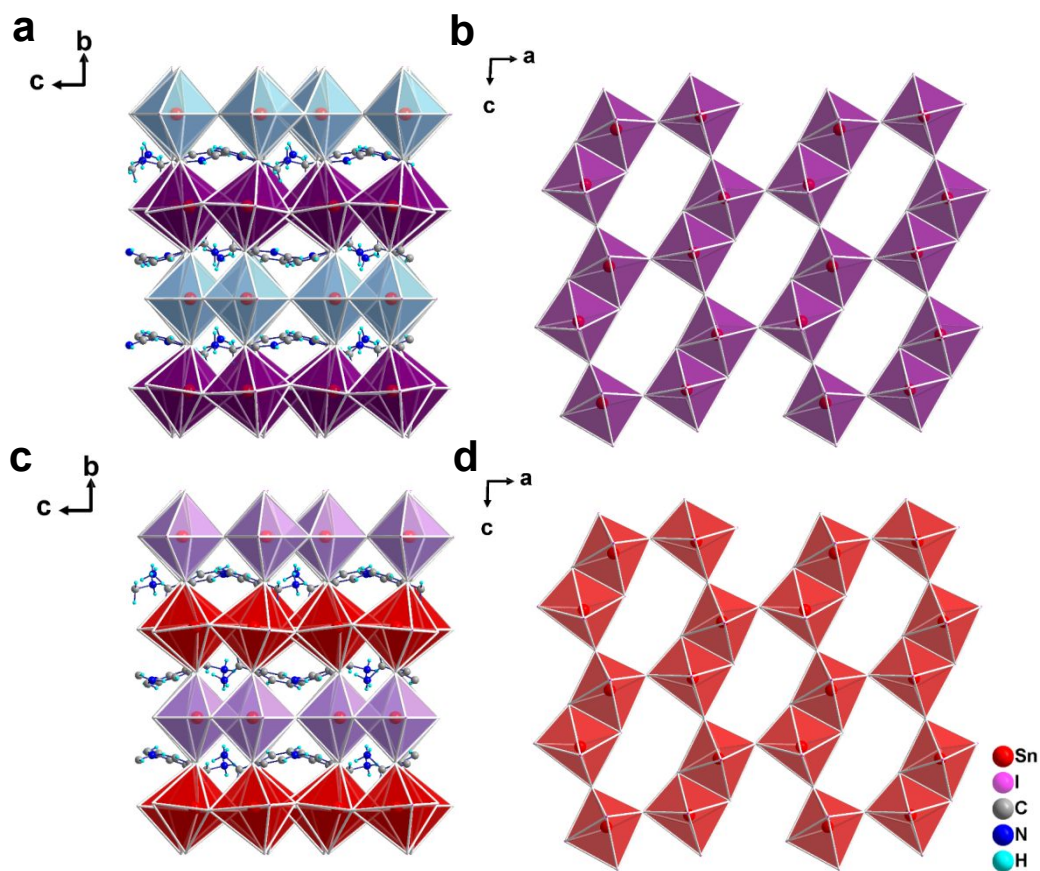


Figure 4. (a) Crystal structure of (3AMPY)Sn<sub>2</sub>I<sub>6</sub>. (b) Connection motif of the octahedra for the bottom layer (organic cations omitted for clarity). (c) Crystal structure of (4AMPY)Sn<sub>2</sub>I<sub>6</sub>. (d) Connection motif of the octahedra for the bottom layer (organic cations omitted for clarity).

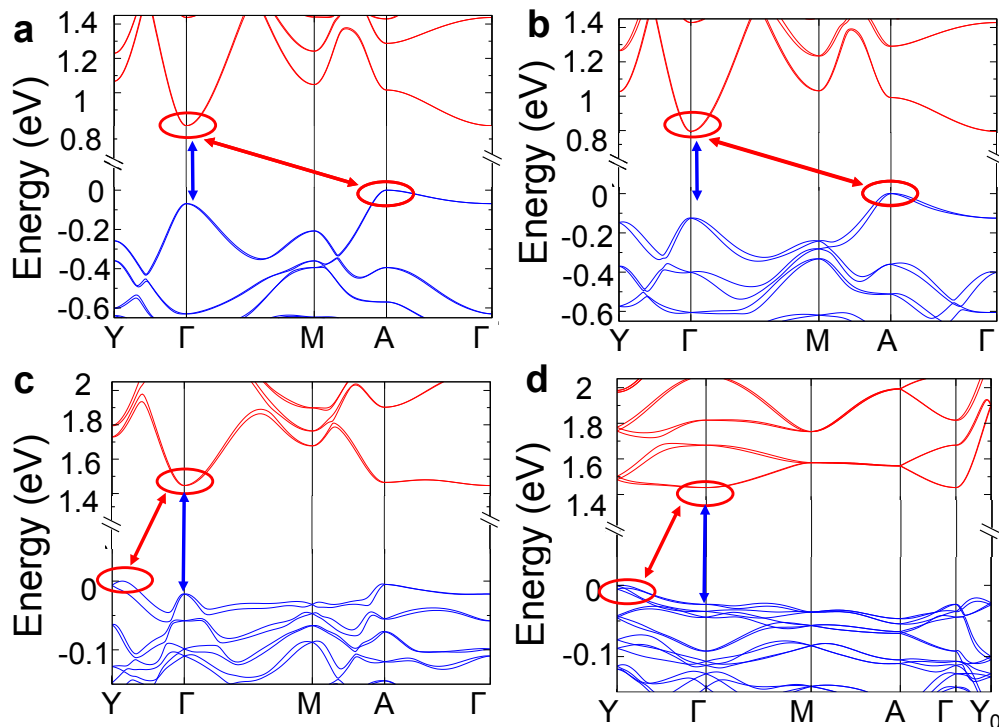


Figure 5. DFT calculations of band structures for (a) (3AMPY)Sn<sub>2</sub>I<sub>6</sub>, (b) (4AMPY)Sn<sub>2</sub>I<sub>6</sub>, (c) (3AMPY)Pb<sub>2</sub>I<sub>6</sub> and (d) (4AMPY)Pb<sub>2</sub>I<sub>6</sub>. The red circles indicate the VBM and CBM. The red arrows indicate the indirect bandgaps while the blue arrows indicate the direct bandgaps.

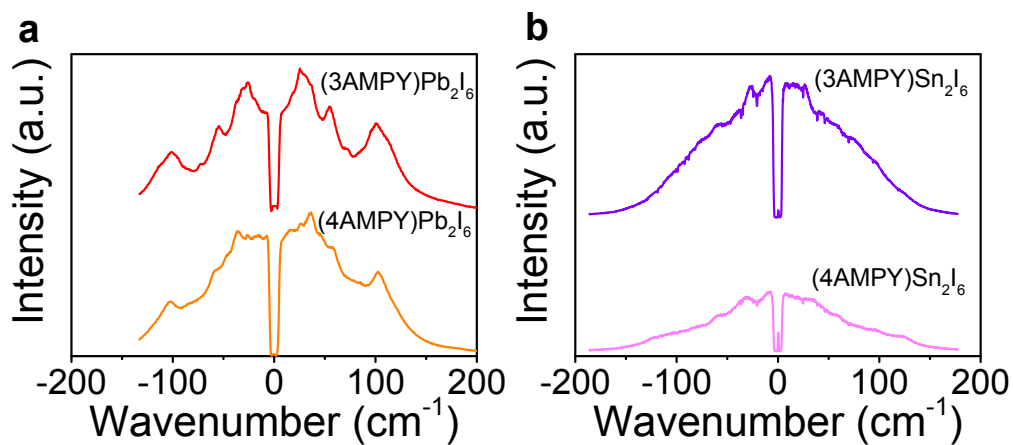


Figure 6. (a) Raman spectra of (3AMPY)Pb<sub>2</sub>I<sub>6</sub> and (4AMPY)Pb<sub>2</sub>I<sub>6</sub>. (b) Raman spectra of (3AMPY)Sn<sub>2</sub>I<sub>6</sub> and (4AMPY)Sn<sub>2</sub>I<sub>6</sub> (room temperature).

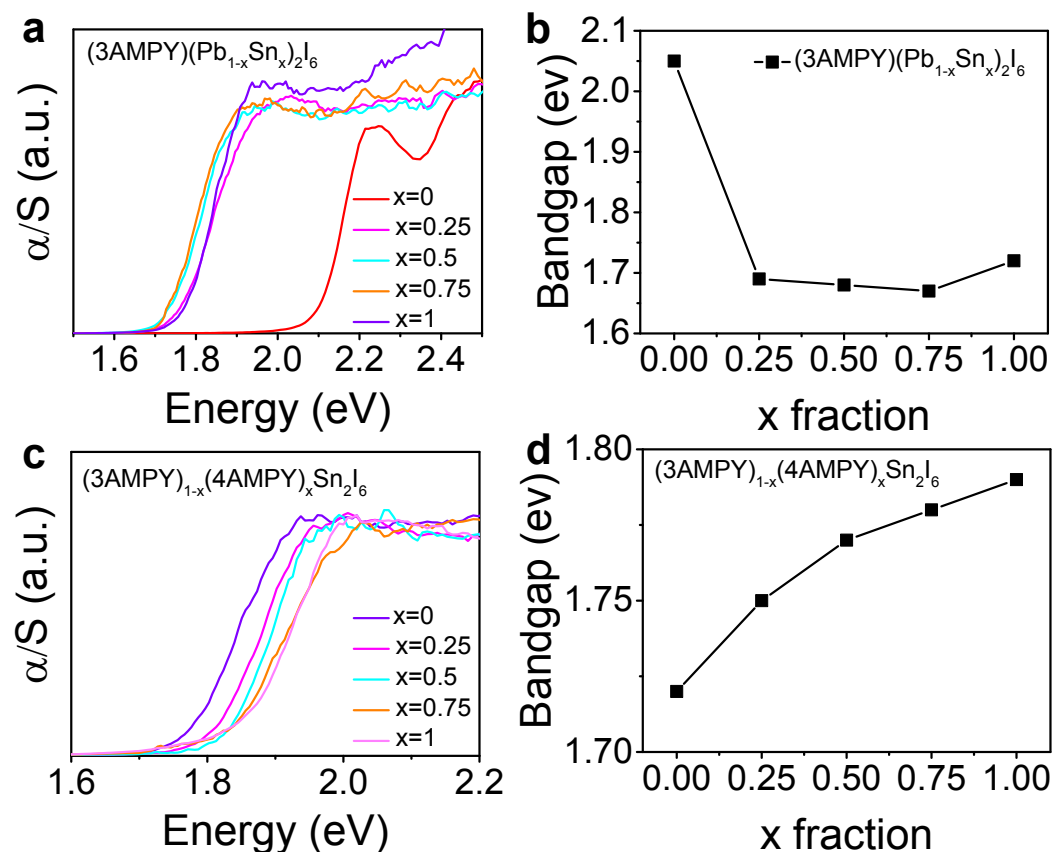


Figure 7. (a) The electronic absorption spectra for the  $(3\text{AMPY})(\text{Pb}_{1-x}\text{Sn}_x)_2\text{I}_6$  series. (b) Bandgaps values extracted from Tauc plots assuming indirect bandgaps (Figure S4a). (c) Electronic absorption spectra for the  $(3\text{AMPY})_{1-x}(\text{4AMPY})_x\text{Sn}_2\text{I}_6$  series. (d) Bandgaps values extracted from Tauc plots assuming indirect bandgaps (Figure S4b). Slightly different band gap values assuming direct electronic band gaps are provided in supporting information (Figure S5).



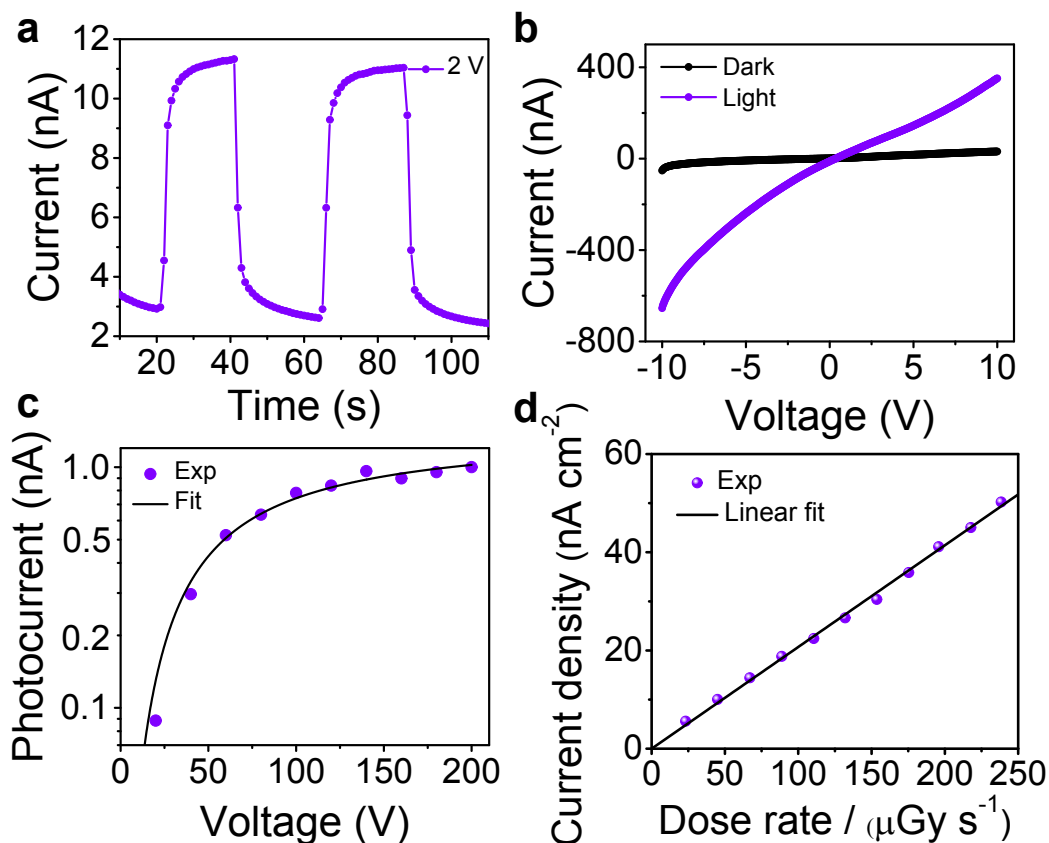


Figure 8. Optoelectronic response of the (3AMPY)Pb<sub>2</sub>I<sub>6</sub> device. (a) On-off switching under ambient light with 2V bias. (b) Current-voltage curve measured from -10 V to 10 V under 10 mW/cm<sup>2</sup> illumination and in the dark. (c) Bias dependent X-ray photocurrent of the (3AMPY)Pb<sub>2</sub>I<sub>6</sub> device under an uncollimated Ag X-ray tube source with a tube voltage of 50 kV. The Many equation was used for fitting. (d) X-ray sensitivity measurement of the (3AMPY)Pb<sub>2</sub>I<sub>6</sub> device under a bias of 200 V. The Ag X-ray tube voltage was 50 kV.

## TOC Graphic

